

TOI-481 b & TOI-892 b: Two long period hot Jupiters from the Transiting Exoplanet Survey Satellite

RAFAEL BRAHM,<sup>1,2</sup> LOUISE D. NIELSEN,<sup>3</sup> ROBERT A. WITTENMYER,<sup>4</sup> SONGHU WANG,<sup>5</sup> JOSEPH E. RODRIGUEZ,<sup>6</sup>  
NÉSTOR ESPINOZA,<sup>7</sup> MATÍAS I. JONES,<sup>8</sup> ANDRÉS JORDÁN,<sup>1,2</sup> THOMAS HENNING,<sup>9</sup> MELISSA HOBSON,<sup>2,10</sup>  
DIANA KOSSAKOWSKI,<sup>9</sup> FELIPE ROJAS,<sup>10,2</sup> PAULA SARKIS,<sup>9</sup> MARTIN SCHLECKER,<sup>9</sup> TRIFON TRIFONOV,<sup>9</sup> SAHAR SHAHAF,<sup>11</sup>  
GEORGE RICKER,<sup>12</sup> ROLAND VANDERSPEK,<sup>12</sup> DAVID W. LATHAM,<sup>6</sup> SARA SEAGER,<sup>12,13,14</sup> JOSHUA N. WINN,<sup>15</sup>  
JON M. JENKINS,<sup>16</sup> BRETT C. ADDISON,<sup>17</sup> GÁSPÁR Á. BAKOS,<sup>15</sup> WAQAS BHATTI,<sup>15</sup> DANIEL BAYLISS,<sup>18</sup> PERRY BERLIND,<sup>6</sup>  
ALLYSON BIERYLA,<sup>6</sup> FRANCOIS BOUCHY,<sup>3</sup> BRENDAN P. BOWLER,<sup>19</sup> CÉSAR BRICEÑO,<sup>20</sup> TIMOTHY M. BROWN,<sup>21,22</sup>  
EDWARD M. BRYANT,<sup>18,23</sup> DOUGLAS A. CALDWELL,<sup>24,25</sup> DAVID CHARBONNEAU,<sup>6</sup> KAREN A. COLLINS,<sup>6</sup> ALLEN B. DAVIS,<sup>5</sup>  
GILBERT A. ESQUERDO,<sup>6</sup> BENJAMIN J. FULTON,<sup>26</sup> NATALIA M. GUERRERO,<sup>12</sup> CHRISTOPHER E. HENZE,<sup>16</sup> ALEISHA HOGAN,<sup>27</sup>  
JONATHAN HORNER,<sup>17</sup> CHELSEA X. HUANG,<sup>12</sup> JONATHAN IRWIN,<sup>6</sup> STEPHEN R. KANE,<sup>28</sup> JOHN KIELKOPF,<sup>29</sup>  
ANDREW W. MANN,<sup>30</sup> TSEVI MAZEH,<sup>31</sup> JAMES MCCORMAC,<sup>18</sup> CURTIS MCCULLY,<sup>22,32</sup> MATTHEW W. MENGEL,<sup>17</sup>  
ISMAEL MIRELES,<sup>12</sup> JACK OKUMURA,<sup>17</sup> PETER PLAVCHAN,<sup>33</sup> SAMUEL N. QUINN,<sup>6</sup> MARKUS RABUS,<sup>34,32</sup> SOPHIE SAESEN,<sup>3</sup>  
JOSHUA E. SCHLIEDER,<sup>35</sup> DAMIEN SEGRANSAN,<sup>3</sup> BERNIE SHIAO,<sup>7</sup> AVI SHPORER,<sup>12</sup> ROBERT J. SIVERD,<sup>36</sup>  
KEIVAN G. STASSUN,<sup>37</sup> VINCENT SUC,<sup>1,38</sup> THIAM-GUAN TAN,<sup>39</sup> PASCAL TORRES,<sup>10,2</sup> CHRIS G. TINNEY,<sup>40</sup> STEPHANE UDRY,<sup>3</sup>  
LEONARDO VANZI,<sup>41,42</sup> MICHAEL VEZIE,<sup>12</sup> JOSE I. VINES,<sup>43</sup> MAJA VUCKOVIC,<sup>44</sup> DUNCAN J. WRIGHT,<sup>17</sup>  
DANIEL A. YAHALOMI,<sup>6</sup> ABNER ZAPATA,<sup>41,42,38</sup> HUI ZHANG,<sup>45</sup> AND CARL ZIEGLER<sup>46</sup>

<sup>1</sup>Facultad de Ingeniera y Ciencias, Universidad Adolfo Ibáñez, Av. Diagonal las Torres 2640, Peñalolén, Santiago, Chile

<sup>2</sup>Millennium Institute for Astrophysics, Chile

<sup>3</sup>Geneva Observatory, University of Geneva, Chemin des Maillettes 51, 1290 Versoix, Switzerland

<sup>4</sup>University of Southern Queensland, Centre for Astrophysics, Toowoomba, QLD 4350, Australia

<sup>5</sup>Department of Astronomy, Yale University, New Haven, CT 06511, USA

<sup>6</sup>Center for Astrophysics | Harvard & Smithsonian, 60 Garden St, Cambridge, MA 02138, USA

<sup>7</sup>Space Telescope Science Institute, 3700 San Martin Drive, Baltimore, MD 21218, USA

<sup>8</sup>European Southern Observatory, Casilla 19001, Santiago, Chile

<sup>9</sup>Max-Planck-Institut für Astronomie, Königstuhl 17, Heidelberg 69117, Germany

<sup>10</sup>Instituto de Astrofísica, Pontificia Universidad Católica de Chile, Av. Vicuña Mackenna 4860, Macul, Santiago, Chile

<sup>11</sup>School of Physics and Astronomy, Tel-Aviv University, Tel Aviv 69978, Israel

<sup>12</sup>Department of Physics and Kavli Institute for Astrophysics and Space Research, Massachusetts Institute of Technology, Cambridge, MA 02139, USA

<sup>13</sup>Department of Earth, Atmospheric and Planetary Sciences, Massachusetts Institute of Technology, Cambridge, MA 02139, USA

<sup>14</sup>Department of Aeronautics and Astronautics, MIT, 77 Massachusetts Avenue, Cambridge, MA 02139, USA

<sup>15</sup>Department of Astrophysical Sciences, Princeton University, NJ 08544, USA

<sup>16</sup>NASA Ames Research Center, Moffett Field, CA 94035, USA

<sup>17</sup>University of Southern Queensland, Centre for Astrophysics, West Street, Toowoomba, QLD 4350 Australia

<sup>18</sup>Dept. of Physics, University of Warwick, Gibbet Hill Road, Coventry CV4 7AL, UK

<sup>19</sup>Department of Astronomy, The University of Texas at Austin, TX 78712, USA

<sup>20</sup>Cerro Tololo Inter-American Observatory, Casilla 603, 1700000, La Serena, Chile

<sup>21</sup>University of Colorado/CASA, Boulder, CO 80309, USA

<sup>22</sup>Las Cumbres Observatory Global Telescope Network, Santa Barbara, CA 93117, USA

<sup>23</sup>Centre for Exoplanets and Habitability, University of Warwick, Gibbet Hill Road, Coventry CV4 7AL, UK

<sup>24</sup>SETI Institute, Mountain View, CA, 94043, USA

<sup>25</sup>SETI Institute/NASA Ames Research Center, Moffett Field, CA 94035, USA

<sup>26</sup>NASA Exoplanet Science Institute / Caltech-IPAC, Pasadena, CA

<sup>27</sup>School of Physics and Astronomy, University of Leicester, University Road, Leicester LE1 7RH, UK

<sup>28</sup>Department of Earth and Planetary Sciences, University of California, Riverside, CA 92521, USA

<sup>29</sup>Department of Physics and Astronomy, University of Louisville, Louisville, KY 40292, USA

<sup>30</sup>Department of Physics and Astronomy, The University of North Carolina at Chapel Hill, Chapel Hill, NC 27599-3255, USA

<sup>31</sup>School of Physics and Astronomy, Raymond and Beverly Sackler Faculty of Exact Sciences, Tel Aviv University, Tel Aviv, 6997801, Israel

<sup>32</sup>*Department of Physics, University of California, Santa Barbara, CA 93106-9530, USA*

<sup>33</sup>*George Mason University, 4400 University Drive MS 3F3, Fairfax, VA 22030, USA*

<sup>34</sup>*Las Cumbres Observatory Global Telescope, 6740 Cortona Dr., Suite 102, Goleta, CA 93111, USA*

<sup>35</sup>*Exoplanets and Stellar Astrophysics Laboratory, Code 667, NASA Goddard Space Flight Center, Greenbelt, MD 20771, USA*

<sup>36</sup>*Gemini Observatory/NSFs NOIRLab, 670 N. Aohoku Place, Hilo, HI, 96720, USA*

<sup>37</sup>*Vanderbilt University, Department of Physics & Astronomy, 6301 Stevenson Center Lane, Nashville, TN 37235, USA*

<sup>38</sup>*El Sauce Observatory, Chile*

<sup>39</sup>*Perth Exoplanet Survey Telescope, Perth, Australia*

<sup>40</sup>*Exoplanetary Science at UNSW, School of Physics, UNSW Sydney, NSW 2052, Australia*

<sup>41</sup>*Department of Electrical Engineering, Pontificia Universidad Católica de Chile, Av. Vicuña Mackenna 4860, 7820436 Macul, Santiago, Chile*

<sup>42</sup>*Center of Astro-Engineering UC, Pontificia Universidad Católica de Chile, Av. Vicuña Mackenna 4860, 7820436 Macul, Santiago, Chile*

<sup>43</sup>*Departamento de Astronomía, Universidad de Chile, Camino El Observatorio 1515, Las Condes, Santiago, Chile*

<sup>44</sup>*Instituto de Física y Astronomía, Universidad de Valparaíso, Casilla 5030, Valparaíso, Chile*

<sup>45</sup>*School of Astronomy and Space Science, Key Laboratory of Modern Astronomy and Astrophysics in Ministry of Education, Nanjing University, Nanjing 210046, Jiangsu, China*

<sup>46</sup>*Dunlap Institute for Astronomy and Astrophysics, University of Toronto, 50 St. George Street, Toronto, Ontario M5S 3H4, Canada*

Submitted to AAS Journals

## ABSTRACT

We present the discovery of two new 10-day period giant planets from the Transiting Exoplanet Survey Satellite (*TESS*) mission, whose masses were precisely determined using a wide diversity of ground-based facilities. TOI-481 b and TOI-892 b have similar radii ( $0.99 \pm 0.01 R_J$  and  $1.07 \pm 0.02 R_J$ , respectively), and orbital periods (10.3311 days and 10.6266 days, respectively), but significantly different masses ( $1.53 \pm 0.03 M_J$  versus  $0.95 \pm 0.07 M_J$ , respectively). Both planets orbit metal-rich stars ( $[Fe/H] = +0.26 \pm 0.05$  dex and  $[Fe/H] = +0.24 \pm 0.05$  for TOI-481 and TOI-892, respectively) but at different evolutionary stages. TOI-481 is a  $M_\star = 1.14 \pm 0.02 M_\odot$ ,  $R_\star = 1.66 \pm 0.02 R_\odot$  G-type star ( $T_{\text{eff}} = 5735 \pm 72$  K), that with an age of 6.7 Gyr, is in the turn-off point of the main sequence. TOI-892 on the other hand, is a F-type dwarf star ( $T_{\text{eff}} = 6261 \pm 80$  K), which has a mass of  $M_\star = 1.28 \pm 0.03 M_\odot$ , and a radius of  $R_\star = 1.39 \pm 0.02 R_\odot$ . TOI-481 b and TOI-892 b join the scarcely populated region of transiting gas giants with orbital periods longer than 10 days, which is important to constrain theories of the formation and structure of hot Jupiters.

*Keywords:* planetary systems — planets and satellites: detectionplanets and satellites: gaseous planets

## 1. INTRODUCTION

Among the vast diversity of extrasolar planets discovered throughout the past three decades, those known as hot Jupiters (e.g., [Mayor & Queloz 1995](#)) are arguably the most well-studied population. These objects are gas giant planets ( $R_P \gtrsim 0.8 R_J$ ) orbiting closely around their host stars, with typical orbital periods shorter than  $\approx 10$  days.

Despite having a relatively low occurrence rate of  $\approx 1\%$  ([Wang et al. 2015](#); [Zhou et al. 2019](#)), due to strong observational biases favoring their detection and characterization, hot Jupiters represent  $\approx 75\%$  of the total sample of

transiting extrasolar planets for which both masses and radii are determined with a precision of at least 20% <sup>1</sup>.

Follow-up observations of hot Jupiters have delivered significant scientific results - including the first studies on the atmospheres of planets outside our own solar system (e.g., [Charbonneau et al. 2002](#); [Vidal-Madjar et al. 2003](#); [Pont et al. 2008](#)); and significant misalignments between orbital and stellar spin axes ([Queloz et al. 2010](#); [Winn et al. 2010](#); [Hébrard et al. 2011](#)).

While in principle the large amount of information available for transiting hot Jupiters should help us in un-

<sup>1</sup> based on the catalogue of the physical properties of transiting planetary systems (TEPCat, [Southworth 2011](#)), updated on July 7, 2020

veiling the formation and evolution mechanisms that allow the existence of close-in gas giants, their extreme environments produced by the proximity to the host stars makes the interpretation of hot Jupiter properties a challenging task (see Dawson & Johnson 2018, for a comprehensive review). The exact formation/migration mechanism of hot Jupiters (e.g., Wu & Lithwick 2011; Beaugé & Nesvorný 2012; Naoz et al. 2012), and the mechanism responsible for generating highly inflated radii (e.g., Bodenheimer et al. 2001; Batygin & Brown 2010; Leconte et al. 2010; Kurokawa & Inutsuka 2015) are some of the active challenges in the field.

Gas giants with orbital periods longer than that of typical hot Jupiters (often called “warm Jupiters”) should not be significantly influenced by these proximity effects, making the orbital and physical characterization of warm Jupiters an important step to solve some of the aforementioned challenges (e.g., Dong et al. 2014; Lopez & Fortney 2016; Thorngren et al. 2016). Ground-based photometric surveys (e.g., Bakos et al. 2004; Pollacco et al. 2006; Pepper et al. 2007; Bakos et al. 2013), which have discovered the vast majority ( $\approx 80\%$ ) of bright transiting hot Jupiter systems, have strong limitations for discovering planets with periods longer than  $P \gtrsim 8$  days (Gaudi et al. 2005). Space based missions such as *Kepler* (Borucki et al. 2010), *Kepler-K2* (Howell et al. 2014), and CoRoT (Auvergne et al. 2009) allowed the discovery and orbital characterization of the first two dozen of such systems (Bonomo et al. 2010; Deeg et al. 2010; Almenara et al. 2018; Shporer et al. 2017; Brahm et al. 2018; Jordán et al. 2019), but due to its significantly larger field of view, the *TESS* mission (Ricker et al. 2015) is expected to significantly increase that number (Sullivan et al. 2015; Barclay et al. 2018). In just its first two years of operation, *TESS* has demonstrated its ability to discover transiting warm Jupiters suitable for characterization follow-up (Nielsen et al. 2019; Huber et al. 2019; Rodriguez et al. 2019; Addison et al. 2020; Gill et al. 2020), and this number will grow with the extended mission (Cooke et al. 2019).

Here we present the discovery and orbital characterization of two gas giants located in the relatively sparsely populated parameter space of orbital periods slightly longer than 10 days. These discoveries were realized in the context of the Warm gIaNts with tEss (WINE) collaboration, which focuses on the systematic characterization of *TESS* transiting warm giant planets (e.g., Brahm et al. 2019; Jordán et al. 2020).

The paper is structured as follows. In Section 2 we present the *TESS* data, and follow-up photometric and spectroscopic observations that allowed the discovery of both planets. In Section 3 we describe the routines

adopted to estimate the stellar parameters of both host stars and the final physical and orbital parameters of TOI-481 b and TOI-892 b. Our findings are discussed in Section 4.

## 2. OBSERVATIONS

### 2.1. *TESS*

TOI-481 and TOI-892 were monitored by *TESS* during its first year of operation. TOI-481 was observed in short cadence (2 minutes) mode in Sectors 6, 7, 9, 10, and 13, and in long cadence (30 minutes) mode in Sector 3. On the other hand, TOI-892 was only observed in Sector 6, in long cadence mode. Transiting candidates were identified on both stars by the *TESS* Science Office, and were released as *TESS* Object of Interest (TOI) to the community. TOI-481 b was identified as a candidate based on two clear “transit-like” features present in the SPOC light curve (Jenkins et al. 2016) of Sector 6. TOI-481 presented a strong detection at  $68\sigma$  and passed all the diagnostic tests conducted and presented in the Data Validation report (Twicken et al. 2018; Li et al. 2019), including the odd/even transit depth test, and the difference image centroiding and ghost diagnostic tests (which help reject false positives due to background sources). No additional transit-like signals were identified in the light curve. On the other hand, TOI-892 b was reported as a *TESS* alert on July 12, 2019 based on the analysis of the quick look pipeline (Huang et al. 2019) of Sector 6. For both candidates the predicted planetary radii were consistent with being Jovian planets with orbital periods close to 10 days.

For the TOI-481 analysis presented in this study, we downloaded the Pre-search Data Conditioning Simple Aperture Photometry light curves (Stumpe et al. 2012) of Sectors 6, 7, 9, 10, and 13 from the Mikulski Archives for Space Telescopes (see Figure 1). Systematic trends were removed from these light curves using the co-trending basis vectors (Smith et al. 2012; Stumpe et al. 2014), generated by the *TESS* SPOC at NASA Ames Research Center. We additionally obtained the long cadence light curve from the Full Frame Images of Sector 3 by using the `tesseract`<sup>2</sup> pipeline. For the analysis of TOI-892, we generated the long cadence light curve from the Full Frame Images of Sector 6 through `tesseract` (see Figure 2). The long cadence light curves for TOI-481 and TOI-892 used in this study are listed in Table 1.

### 2.2. *Ground-based photometry*

<sup>2</sup> <https://github.com/astrofelipe/tesseract>

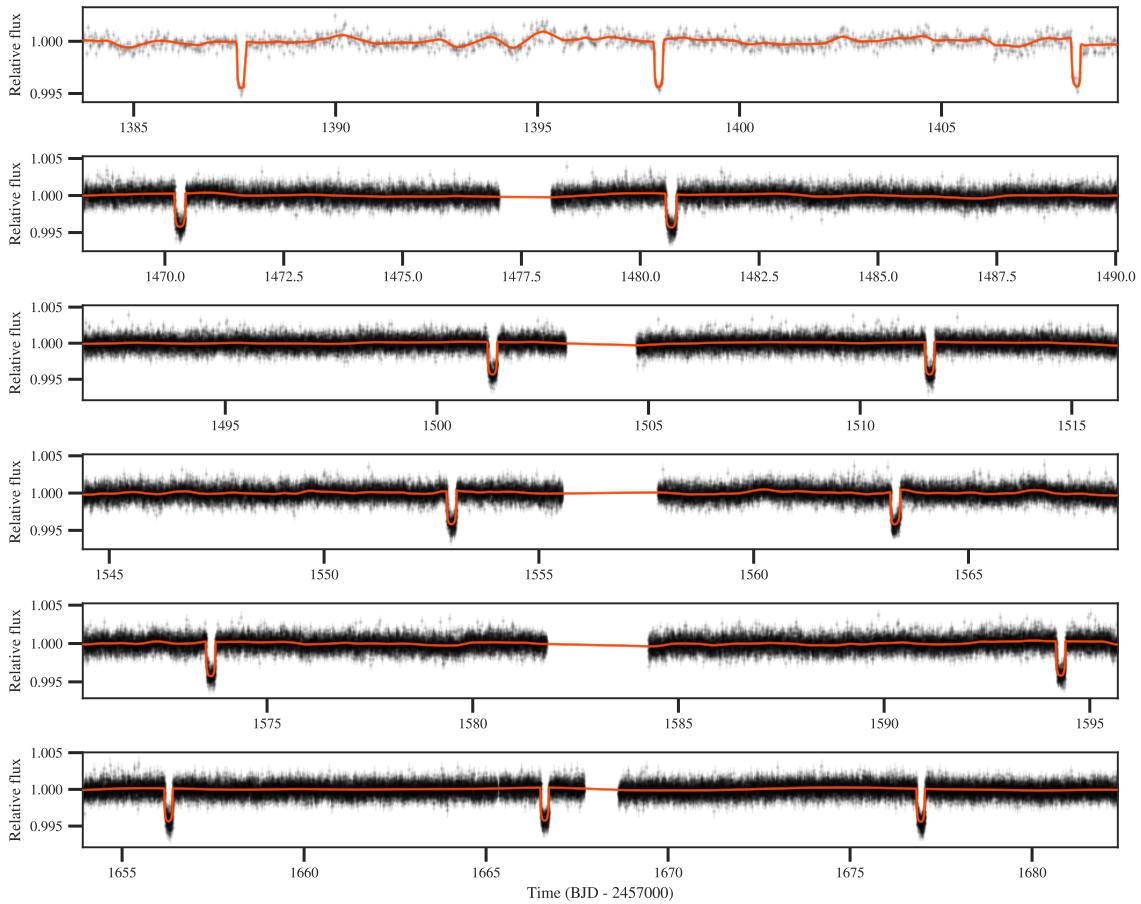


**Figure 1.** TOI-481 light curves of the six *TESS* Sectors used in our analysis. The top panel presents the *TESS* Sector 3 data from the Full Frame Images as black points with errorbars obtained with `tesseract` (see text), while the rest of the panels show the 2-minute cadence Pre-search Data Conditioning Simple Aperture Photometry light curves for Sectors 6, 7, 9, 10 and 13, respectively. The orange line corresponds to the model obtained in Section 3, which consists of a transit model combined with a Gaussian process that describes the remaining flux variability.

The limited spatial resolution of the *TESS* mission and its relatively large pixel scale ( $21''/\text{pix}$ ) makes necessary the execution of ground-based photometric observations to confirm that the transit features occur on target and not on close neighbor stars. Transits of both candidates were monitored with three different ground-based facilities installed in Chile. These observations were performed in the context of the *TESS* Follow-up Observing Program (TFOP) Working Group Sub Group 1 (SG1). The four photometric timeseries are publicly available on the Exoplanet Follow-up Observing Program for *TESS* (ExoFOP-*TESS*) website<sup>3</sup>.

### 2.2.1. CHAT

The Chilean Hungarian Automated Telescope<sup>4</sup> (CHAT) is a robotic facility installed at Las Campanas Observatory in Chile. CHAT consists in a FORNAX 200 equatorial mount, and a 0.7 m telescope coupled to a FLI ML-23042 CCD of  $2048 \times 2048$  pixels, which delivers a pixel scale of  $0.6''/\text{pix}$ . CHAT contains a set of  $i'$ ,  $r'$ , and  $g'$  passband filters.

TOI-481 was observed with CHAT on the night of March 30, 2019 with the  $i'$  filter adopting an exposure time of 20 s. We obtained 516 images of TOI-481 with airmass values between 1.2 and 2. CHAT data were processed with a dedicated pipeline that performs differential aperture photometry, where the optimal comparison sources and the radius of the photometric aperture are automatically selected (e.g., Espinoza et al. 2019; Jones

<sup>3</sup> <https://exofop.ipac.caltech.edu/tess>

<sup>4</sup> [https://www.exoplanetscience2.org/sites/default/files/submission-attachments/poster\\_aj.pdf](https://www.exoplanetscience2.org/sites/default/files/submission-attachments/poster_aj.pdf)

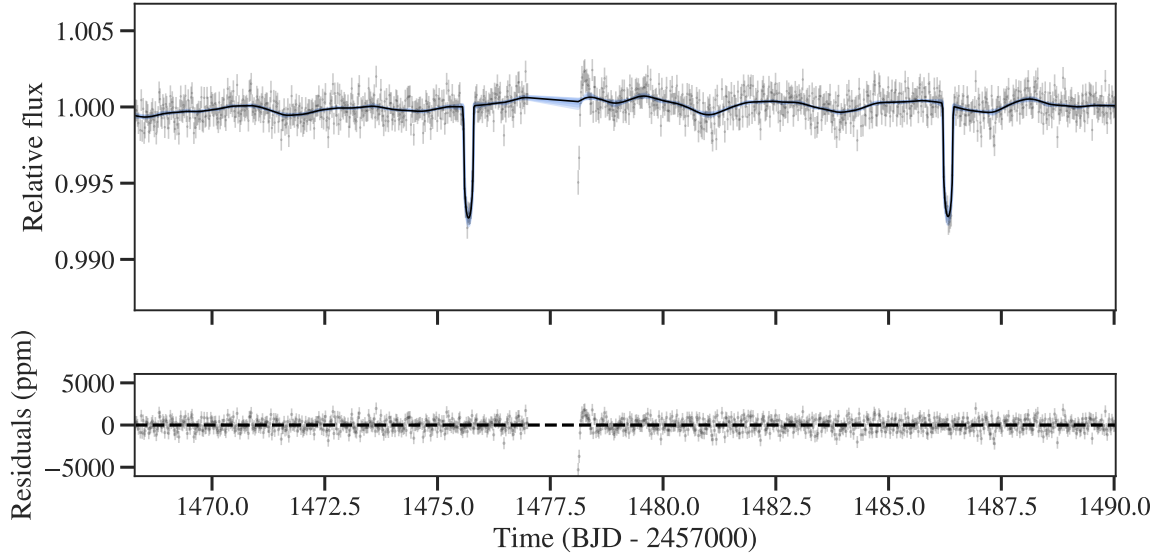


**Figure 2.** The top panel corresponds to the TESS 30 minutes cadence light curve of TOI-892 generated through `tesseract` from the Full Frame Images of Sector 6. The solid line corresponds to the model generated from the posterior parameters of the analysis presented in Section 3. The bottom panel shows the residuals between the *TESS* light curve and the model.

**Table 1.** Long cadence (30 minutes) *TESS* light curve data for TOI-481 and TOI-892 obtained from the `tesseract` extraction of the Full Frame Images of Sector 3 and 6, respectively .

| ID      | BJD               | Flux    | $\sigma_{\text{Flux}}$ | Sector |
|---------|-------------------|---------|------------------------|--------|
| TOI-481 | 2458382.051879883 | 25279.4 | 4.8                    | 3      |
| TOI-481 | 2458382.072692871 | 25272.1 | 4.7                    | 3      |
| TOI-481 | 2458382.093566895 | 25274.6 | 4.7                    | 3      |
| TOI-481 | 2458382.114379883 | 25282.0 | 4.7                    | 3      |
| TOI-481 | 2458382.135192871 | 25279.4 | 4.7                    | 3      |
| TOI-481 | 2458382.156066895 | 25277.6 | 4.7                    | 3      |
| TOI-481 | 2458382.176940918 | 25283.0 | 4.7                    | 3      |
| TOI-481 | 2458382.197753906 | 25282.9 | 4.7                    | 3      |
| TOI-481 | 2458382.218566895 | 25277.7 | 4.7                    | 3      |
| TOI-481 | 2458382.239440918 | 25299.6 | 4.7                    | 3      |

NOTE— This table is available in a machine-readable form in the online journal. A portion is shown here for guidance regarding its form and content.

et al. 2019; Jordán et al. 2019). The light curve obtained is presented in the left panel of Figure 3 and shows an ingress for TOI-481 b which confirms that the transit identified in *TESS* data occurs in a region of  $8''$  centered on TOI-481.

TOI-892 was photometrically monitored with CHAT on the night of November 27, 2019. The *i'* filter was used

to obtain 189 images with an exposure time of 66 s. The right panel of Figure 3 presents the CHAT light curve obtained for TOI-892 b, where a  $\approx 7000$  ppm egress can be identified, ensuring that the transit occurs inside  $6''$  from TOI-892.

### 2.2.2. M<sub>Earth</sub>-South

The M<sub>Earth</sub>-South project (Irwin et al. 2015) consists in an array of eight identical robotic 0.4 m telescopes installed in the Cerro Tololo International Observatory, in Chile. Seven telescopes of the array were used to monitor a transit of TOI-892 b the night of February 20, 2020. Each of the telescopes obtained approximately 360 images with a cadence of 52 s using a custom made RG715 filter. The data were processed with the M<sub>Earth</sub> South pipeline producing the light curve displayed in Figure 3, which further confirms the occurrence of the transit on target by registering an ingress.

### 2.2.3. NGTS

The Next Generation Transit Survey (NGTS, Wheatley et al. 2018) is an array of twelve identical robotic telescopes installed at the Paranal Observatory in Chile. Four NGTS telescopes were used simultaneously on the night of December 3, 2019 to monitor an egress of TOI-481 b. Exposures were taken using a custom NGTS filter (520-890 nm) with 10 s exposure times which resulted in a  $\sim 12$  s cadence. Data were reduced using the NGTS aperture photometry pipeline detailed in Bryant et al. (2020). The NGTS light curve is presented in Figure 3.

## 2.3. High resolution imaging

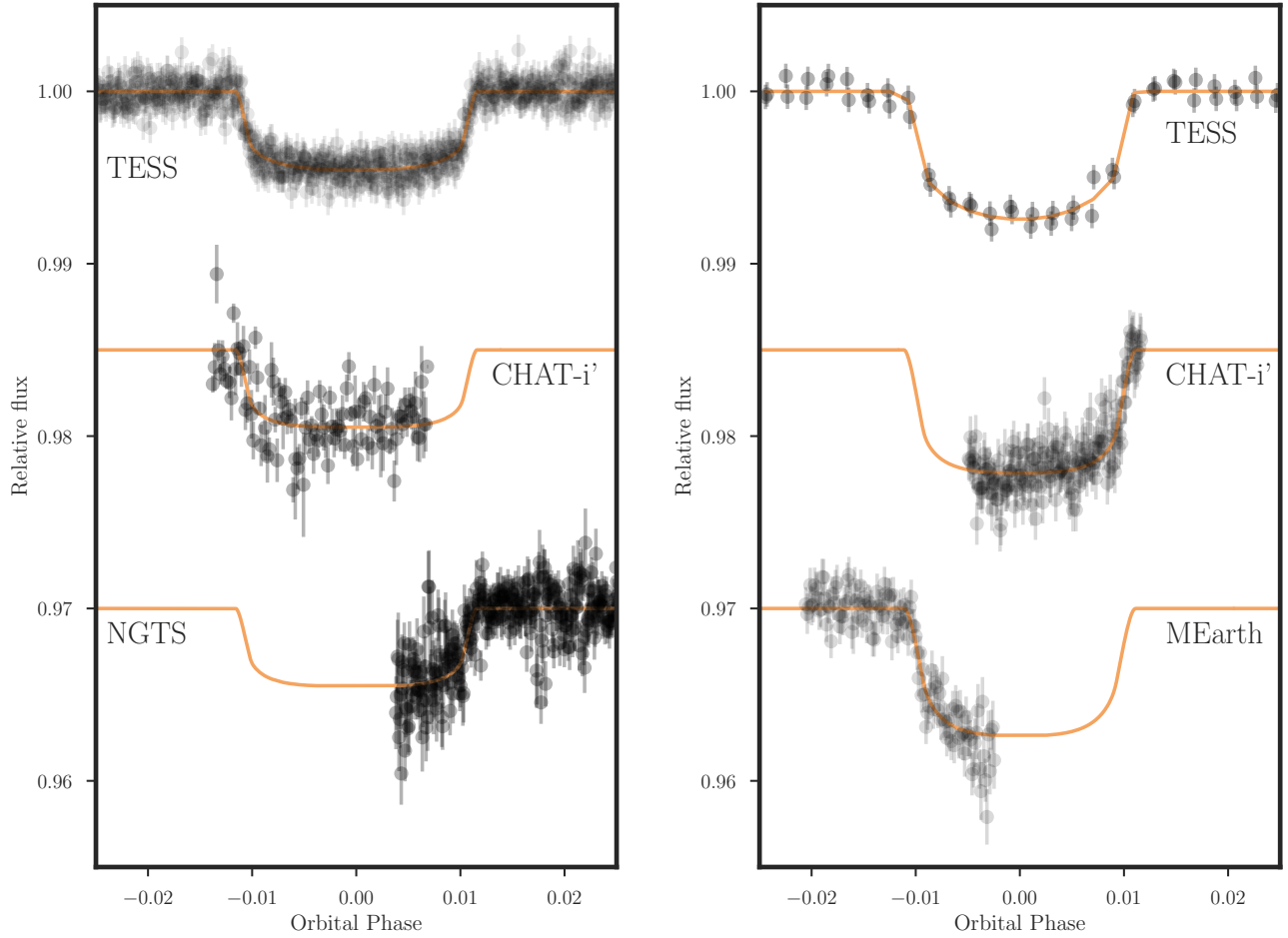


**Figure 3.** The left panel shows the phase folded 2 minute cadence *TESS* photometry of TOI-481 along with the ground-based follow-up light curves of CHAT and NGTS. The solid line shows the corresponding transit model in each case. The right panel shows the phase folded *TESS* long cadence, CHAT, and MEarth light curves for TOI-892.

The identification of contaminating sources in the neighborhood of transiting candidates is important for constraining false positive scenarios and for determining possible dilutions of the transits. In this context, TOI-481 and TOI-892 were imaged with the High-Resolution Camera (HRCam) installed at the 4.1m Southern Astrophysical Research (SOAR, Tokovinin 2018) telescope, in Cerro Pachón, Chile. Observations took place on the night of November 9, 2019, in the context of the SOAR *TESS* Survey (Ziegler et al. 2020). No nearby sources were detected in the vicinity of either star (see Figure 4).

We also used the Gaia DR2 catalog (Gaia Collaboration et al. 2018) to identify the presence of close companions that could dilute the transit depths of TOI-481 b and TOI-892 b obtained from the ground-based light curves presented in section 2.2. We find that inside  $10''$  from the target, TOI-481 contains just one source having a magnitude difference of 8.7 mag in the G passband filter, which is too faint to significantly affect the transit

depth of TOI-481 b. TOI-892 reports no nearby sources closer than  $10''$  to it.

#### 2.4. High resolution spectroscopy

TOI-481 and TOI-892 were monitored with seven different spectrographs with the goal of measuring radial velocity variations to confirm the planetary nature of the transiting candidates and constrain their orbital parameters and masses. These observations are described in the following paragraphs and the radial velocities are presented in Table 2 and displayed in Figure 5.

##### 2.4.1. FEROS

The Fiberfed Extended Range Optical Spectrograph (FEROS, Kaufer et al. 1999) has a resolving power of  $R=48,000$  and is installed on the MPG2.2 m telescope at La Silla Observatory, in Chile. For this study, all FEROS data were processed with the CERES pipeline (Brahm et al. 2017a), which delivers optimally extracted, wavelength calibrated, and instrumental drift

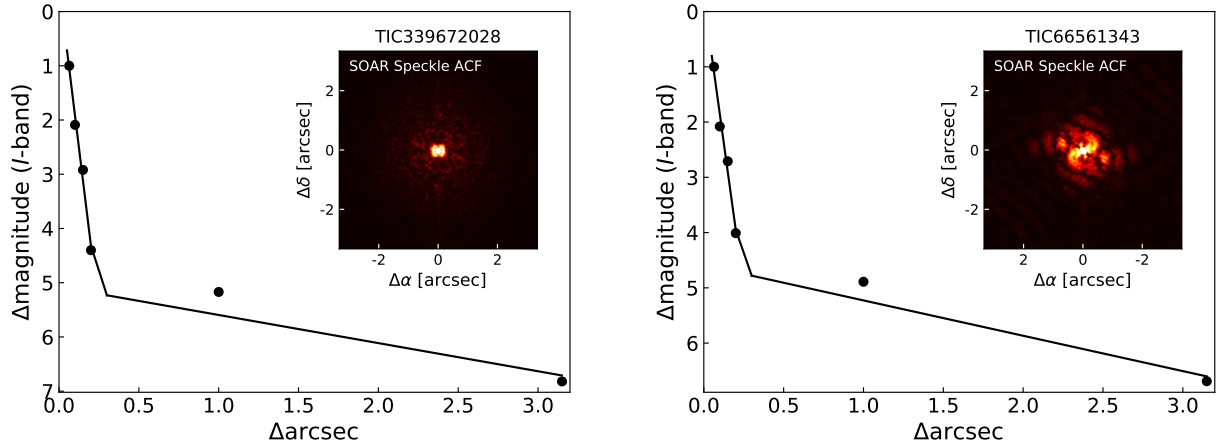


**Figure 4.** Contrast curve plots and auto-correlation functions from Speckle imaging in the I-band using the HRcam at SOAR, for TOI-481 (left panel) and TOI-892 (right panel). The black points correspond to the  $5\sigma$  contrast curve for each star. The solid line is the linear fit to the data for separations  $<0.2''$  and  $>0.2''$ .

corrected spectra, along with the radial velocity and bisector span measurements.

We obtained 16 spectra with FEROS of TOI-481 over a time span of 30 days starting on the night of February 28, 2019. We adopted an exposure time of 300 s which generated spectra with a signal-to-noise ratio per resolution element of  $\sim 110$ .

For TOI-892 we obtained 15 FEROS spectra between November 9, 2019 and March 14, 2020. In this case the exposure time was 900 s and the obtained spectra reached a typical signal-to-noise ratio per resolution element of  $\sim 80$ .

In both cases we used the simultaneous calibration technique by taking a spectrum of a Thorium-Argon lamp with the comparison fiber to trace the instrumental drift during the science exposure.

#### 2.4.2. CHIRON

The CHIRON instrument (Tokovinin et al. 2013) is a high-resolution and fiber-fed spectrograph mounted on the 1.5 m Smarts telescope at CTIO, Chile. We collected a total of 13 spectra of TOI-481 with CHIRON, between March 8 and April 10, 2019. For this object we used the image slicer mode ( $R=80,000$ ), with exposure times between 750 and 1200 s, leading to a mean signal-to-noise per pixel of 33. From this dataset, we computed precision radial velocities following the method described in Wang et al. (2019), Jones et al. (2019) and Jordán et al. (2020). We achieve a mean radial velocity precision of  $9 \text{ m s}^{-1}$ .

#### 2.4.3. TRES

The Tillinghast Reflector Echelle Spectrograph (TRES; Fűrész 2008)<sup>5</sup> is a  $R=44,000$  fiber fed instrument mounted on the 1.5 m Tillinghast Reflector at the Fred L. Whipple Observatory (FLWO) on Mt. Hopkins, AZ. TRES was used to obtain 14 spectra of TOI-892 between October 7, 2019 and January 28, 2020. A full description of the reduction pipeline and radial velocity extraction process can be seen in Buchhave et al. (2010). We deviate from this methodology in the creation of the reference template used for the cross-correlation. We created a high signal-to-noise template spectrum by shifting and median-combining all the spectra, and cross-correlating each observed spectrum against this template to determine the final radial velocities.

The TRES spectra of TOI-892 were analyzed using the Stellar Parameter Classification (SPC) package (Buchhave et al. 2012). From this analysis, we estimated the effective temperature, metallicity, surface gravity, and rotational velocity of TOI-892 to be:  $T_{\text{eff}} = 6048 \pm 50 \text{ K}$ ,  $\log g_{\star} = 4.32 \pm 0.11 \text{ dex}$ ,  $[\text{Fe}/\text{H}] = +0.32 \pm 0.08 \text{ dex}$ , and  $v \sin i = 8.2 \pm 0.5 \text{ km s}^{-1}$ .

#### 2.4.4. CORALIE

CORALIE is a high resolution ( $R=60,000$ ) fiber-fed spectrograph mounted on the 1.2 m Swiss Euler telescope at La Silla Observatory, Chile. CORALIE is a stabilized instrument with a comparison fiber to trace the instrumental variations during scientific exposures. We obtained 9 CORALIE spectra of TOI-481 between March 1, 2019 and April 4, 2019 using a Fabry-Perot as wavelength comparison source. The CORALIE data were processed with its standard data reduction soft-

<sup>5</sup> <http://www.sao.arizona.edu/html/FLWO/60/TRES/GABORthesis.pdf>

ware, where radial velocities and line bisector spans are computed via cross-correlation with a G2 binary mask. In an exposure time of 1200 - 1800 s we obtain signal-to-noise ratio per resolution element of about 30 in individual spectra, corresponding to a final radial velocity uncertainty of  $\sim 10 \text{ m s}^{-1}$ .

#### 2.4.5. MINERVA-Australis

MINERVA-Australis is an array of four PlaneWave CDK700 telescopes which can be simultaneously fiber-fed to a single KiwiSpec R4-100 high-resolution ( $R=80,000$ ) spectrograph (Barnes et al. 2012; Addison et al. 2019, 2020). TOI-481 was monitored by MINERVA-Australis using one and/or two telescopes in the array (MINERVA3 and MINERVA4) between March 1, 2019 and May 23, 2019, obtaining 54 spectra in the process over 22 different epochs. Radial velocities for the observations are derived for each telescope by cross-correlation, where the template being matched is the mean spectrum of each telescope. The instrumental variations are corrected by using simultaneous Thorium-Argon arc lamp observations. Radial velocities computed from different MINERVA telescopes are modeled in Section 3.3 as originating from independent instruments.

#### 2.4.6. NRES

Las Cumbres Observatory’s (Brown et al. 2013) Network of Robotic Echelle Spectrographs (NRES, Siverd et al. 2018) is a global array of echelle spectrographs mounted on 1 m telescopes, with a resolving power of  $R \approx 53,000$ . TOI-481 was observed with the NRES node located at the South African Astronomical Observatory, for 9 nights between March and April, 2019. At each observing epoch, two or three consecutive exposures were obtained with a total nightly exposure time of 3600 s. Overall, 21 spectra were obtained, with an individual signal-to-noise ratio per resolution element larger than 30.

A SpecMatch (Yee et al. 2017) analysis was performed on the NRES spectra and yielded  $T_{\text{eff}} = 5730 \pm 100 \text{ K}$ ,  $\log g = 3.9 \pm 0.1 \text{ dex}$ ,  $[\text{Fe}/\text{H}] = +0.34 \pm 0.06 \text{ dex}$  and  $v \sin i \lesssim 2 \text{ km s}^{-1}$ . The radial velocity of each exposure was derived via cross-correlation with a PHOENIX template (Husser et al. 2013) with  $T_{\text{eff}} = 5700 \text{ K}$ ,  $\log g = 4.0 \text{ dex}$ ,  $[\text{Fe}/\text{H}] = +0.5 \text{ dex}$ , and  $v \sin i = 2 \text{ km s}^{-1}$ . Systematic drifts were corrected per order (e.g., Engel et al. 2017).

### 3. ANALYSIS

#### 3.1. Properties of the host star

We used the co-added FEROS spectra of TOI-481 and TOI-892 to obtain their respective atmospheric parameters. They were obtained using the ZASPE code (Brahm

**Table 2.** Radial velocity measurements for TOI-481 and TOI-892.

| ID      | BJD        | RV                    | $\sigma_{\text{RV}}$  | Instrument |
|---------|------------|-----------------------|-----------------------|------------|
|         | -2450000   | ( $\text{m s}^{-1}$ ) | ( $\text{m s}^{-1}$ ) |            |
| TOI-481 | 8543.59063 | 37723.80              | 5.40                  | FEROS      |
| TOI-481 | 8544.41789 | 37227.70              | 41.69                 | NRES       |
| TOI-481 | 8544.43251 | 37253.27              | 143.99                | NRES       |
| TOI-481 | 8544.44711 | 37203.45              | 123.13                | NRES       |
| TOI-481 | 8544.69135 | 37672.30              | 9.40                  | CORALIE    |
| TOI-481 | 8544.69945 | 37690.60              | 9.40                  | FEROS      |
| TOI-481 | 8545.41809 | 37032.61              | 120.31                | NRES       |
| TOI-481 | 8545.43966 | 37015.83              | 72.10                 | NRES       |
| TOI-481 | 8546.69284 | 37714.30              | 6.30                  | FEROS      |
| TOI-481 | 8548.68585 | 37823.70              | 5.50                  | FEROS      |

NOTE— This table is available in a machine-readable form in the online journal. A portion is shown here for guidance regarding its form and content.

et al. 2017b). ZASPE works by comparison via  $\chi^2$  minimization of the observed spectrum with a grid of synthetic models generated from the ATLAS9 model atmospheres (Castelli & Kurucz 2003). The evaluation is performed in a subset of spectral regions that are most sensitive to changes in the atmospheric parameters. The errors on the atmospheric parameters are computed through Monte Carlo simulations where the depth of the absorption lines of the synthetic models are randomly perturbed to account for the systematic model mismatch. For TOI-481 we obtain an effective temperature of  $T_{\text{eff}} = 5735 \pm 72 \text{ K}$ , a surface gravity of  $\log g = 4.06^{+0.01}_{-0.01} \text{ dex}$ , a metallicity of  $[\text{Fe}/\text{H}] = +0.26 \pm 0.05 \text{ dex}$ , and a projected rotational velocity of  $v \sin i = 4.54 \pm 0.3 \text{ km s}^{-1}$ . On the other hand, for TOI-892 we found the following set of atmospheric parameters:  $T_{\text{eff}} = 6261 \pm 80 \text{ K}$ ,  $\log g = 4.26^{+0.02}_{-0.02} \text{ dex}$ ,  $[\text{Fe}/\text{H}] = +0.24 \pm 0.05 \text{ dex}$ , and  $v \sin i = 7.69 \pm 0.5 \text{ km s}^{-1}$ .

For estimating the stellar physical parameters we followed the same procedure presented in Brahm et al. (2019). Briefly, we use the PARSEC isochrones (Bressan et al. 2012) containing the Gaia (G,  $G_{\text{BP}}$ ,  $G_{\text{RP}}$ ) and 2MASS absolute magnitudes for a given set of stellar mass, age and metallicity. We then use the spectroscopic temperature, the observed magnitudes and the Gaia parallax as data to estimate the stellar mass and the age of each system through a Monte Carlo Markov Chain (MCMC) exploration of the parameter space. We fix the metallicity of the isochrones to the value ob-



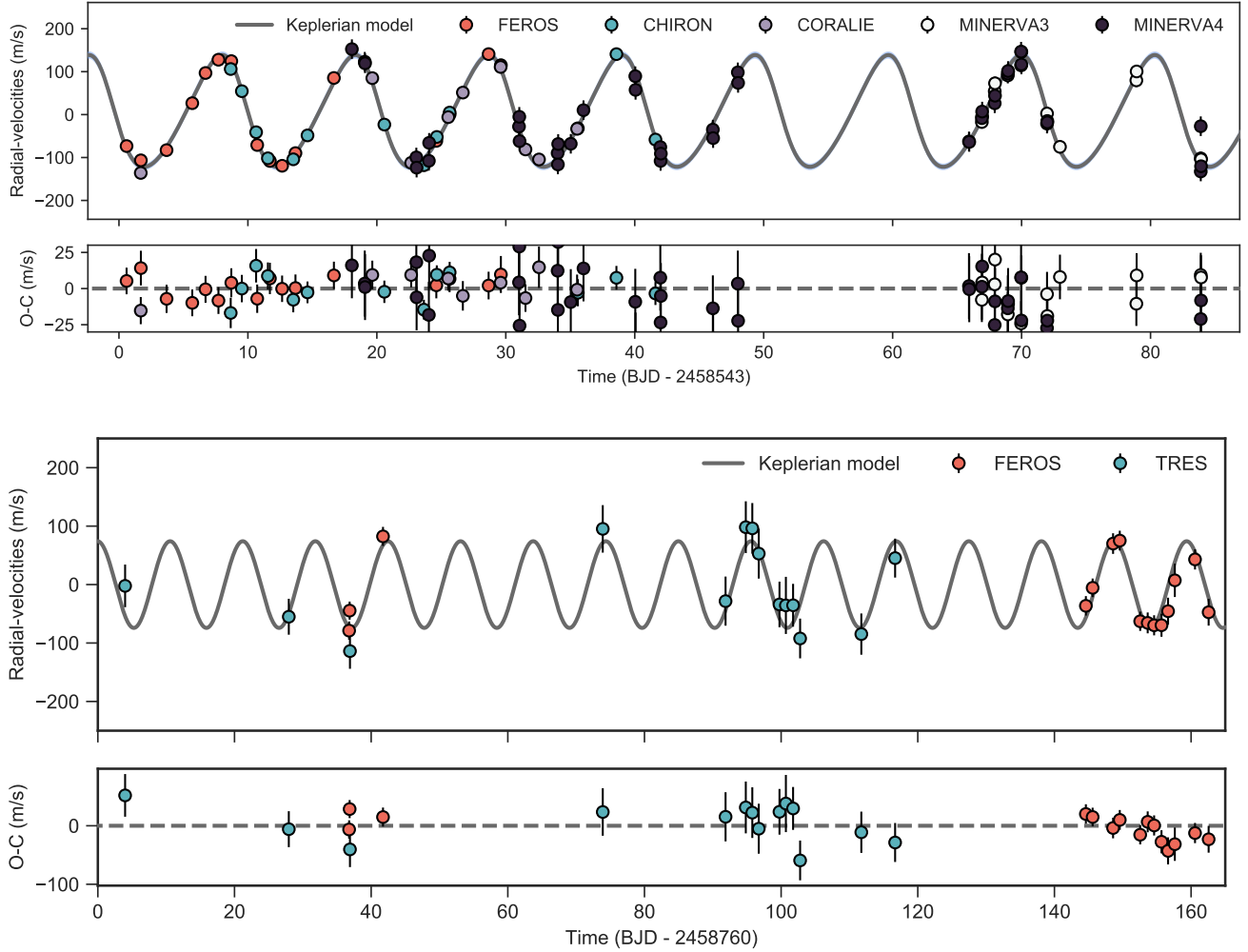


**Figure 5.** Radial velocity observations for TOI-481 (top panel) and TOI-892 (bottom panel). The solid line corresponds to a Keplerian model using the posterior parameters of the global modeling presented in Section 3. The residuals are also presented below the radial velocity curves for each system. The radial velocity measurements for NRES have been excluded from the plots due to their significantly larger error bars.

tained with ZASPE. With this procedure for TOI-481 we obtained a mass of  $M_{\star} = 1.14^{+0.02}_{-0.01} M_{\odot}$ , a stellar radius of  $R_{\star} = 1.66^{+0.02}_{-0.02} R_{\odot}$ , and an age of  $6.7^{+0.4}_{-0.6}$  Gyr. These parameters indicate that TOI-481 is in the final stages of its main sequence lifetime, about to exhaust the hydrogen in its core. In the case of TOI-892 we obtained a mass of  $M_{\star} = 1.28^{+0.03}_{-0.02} M_{\odot}$ , a stellar radius of  $R_{\star} = 1.39^{+0.02}_{-0.02} R_{\odot}$ , and an age of  $2.2^{+0.5}_{-0.5}$  Gyr. TOI-892 is therefore a metal rich main sequence F-type star. We stress that the uncertainties reported for the stellar physical parameters are internal, and do not account for possible systematic errors associated to the theoretical isochrones.

All atmospheric and physical parameters for both stars are presented in Table 3 along with their photometric magnitudes and other observable properties. Ad-

ditionally, Figure 6 shows how the distributions for the stellar radius and effective temperature compared to the PARSEC stellar evolutionary models.

We also applied the routines presented in Stassun et al. (2018a,b) to obtain an independent set of stellar parameters for TOI-481 and TOI-892. Here we used the Gaia DR2 parallax, along with the  $BVgri$  magnitudes from APASS, the  $JHK_S$  magnitudes from 2MASS, the  $W1-W4$  magnitudes from WISE, and the  $G, G_{BP}, G_{RP}$  magnitudes from Gaia, to perform a spectral energy distribution fit. This method allow us to determine the stellar radius, metallicity, effective temperature, and surface gravity. All parameters obtained through this method are consistent at one sigma to those listed in Table 3.

### 3.2. Radial Velocities

**Table 3.** Stellar properties of TOI-481 and TOI-892.

| Parameter                                  | TOI-481  | TOI-892  | Reference               |
|--|--|--|-------------------------|
| Names .....                                | TIC 339672028<br>2MASS J07220299-5723054<br>TYC 8559-00623-1 | TIC 66561343<br>UCAC4 394-009979<br>TYC 5351-00283-1 | TICv8<br>2MASS<br>TYCHO |
| RA ..... (J2015.5)                         | 07h22m03.04s   | 05h46m57.17s   | TICv8                   |
| DEC ... (J2015.5)                          | -57d23m05.99a  | -11d14m07.22s  | TICv8                   |
| pm <sup>RA</sup> (mas yr <sup>-1</sup> )   | 25.68 ± 0.06   | -0.14 ± 0.09   | Gaia DR2                |
| pm <sup>DEC</sup> (mas yr <sup>-1</sup> )  | -25.38 ± 0.08  | 5.97 ± 0.10  | Gaia DR2                |
| π ..... (mas)                              | 5.55 ± 0.03  | 2.91 ± 0.04  | Gaia DR2                |
| T ..... (mag)                              | 9.393 ± 0.006  | 10.974 ± 0.030                                       | TICv8                   |
| B ..... (mag)                              | 10.68 ± 0.05   | 12.06 ± 0.04   | APASS <sup>a</sup>      |
| V ..... (mag)                              | 10.04 ± 0.02   | 11.45 ± 0.02   | APASS                   |
| G ..... (mag)                              | 9.846 ± 0.002  | 11.343 ± 0.002                                       | Gaia DR2 <sup>b</sup>   |
| G <sub>BP</sub> ..... (mag)                | 10.219 ± 0.005   | 11.643 ± 0.005                                       | Gaia DR2                |
| G <sub>RP</sub> ..... (mag)                | 9.354 ± 0.004  | 10.907 ± 0.003                                       | Gaia DR2                |
| J ..... (mag)                              | 8.80 ± 0.02  | 10.46 ± 0.03   | 2MASS <sup>c</sup>      |
| H ..... (mag)                              | 8.48 ± 0.04  | 10.19 ± 0.02   | 2MASS                   |
| K <sub>s</sub> ..... (mag)                 | 8.443 ± 0.02   | 10.11 ± 0.02   | 2MASS                   |
| T <sub>eff</sub> ..... (K)                 | 5735 ± 72  | 6261 ± 80  | This work               |
| log g ..... (dex)                          | 4.06 <sup>+0.01</sup> <sub>-0.01</sub>                       | 4.26 <sup>+0.02</sup> <sub>-0.02</sub>               | This work               |
| [Fe/H] ..... (dex)                         | +0.26 ± 0.05   | +0.24 ± 0.05   | This work               |
| v sin i ..... (km s <sup>-1</sup> )        | 4.54 ± 0.3   | 7.69 ± 0.5   | This work               |
| M <sub>★</sub> ..... (M <sub>☉</sub> )     | 1.14 <sup>+0.02</sup> <sub>-0.01</sub>                       | 1.28 <sup>+0.03</sup> <sub>-0.02</sub>               | This work               |
| R <sub>★</sub> ..... (R <sub>☉</sub> )     | 1.66 <sup>+0.02</sup> <sub>-0.02</sub>                       | 1.39 <sup>+0.02</sup> <sub>-0.02</sub>               | This work               |
| L <sub>★</sub> ..... (L <sub>☉</sub> )     | 2.72 <sup>+0.10</sup> <sub>-0.08</sub>                       | 2.7 <sup>+0.1</sup> <sub>-0.1</sub>                  | This work               |
| A <sub>V</sub> ..... (mag)                 | 0.06 <sup>+0.05</sup> <sub>-0.04</sub>                       | 0.18 <sup>+0.07</sup> <sub>-0.08</sub>               | This work               |
| Age ..... (Gyr)                            | 6.7 <sup>+0.4</sup> <sub>-0.6</sub>                          | 2.2 <sup>+0.5</sup> <sub>-0.5</sub>                  | This work               |
| ρ <sub>★</sub> ..... (g cm <sup>-3</sup> ) | 0.36 <sup>+0.01</sup> <sub>-0.01</sub>                       | 0.67 <sup>+0.04</sup> <sub>-0.03</sub>               | This work               |

NOTE—<sup>a</sup>Munari et al. (2014), <sup>b</sup>Gaia Collaboration et al. (2018), <sup>c</sup>Skrutskie et al. (2006)

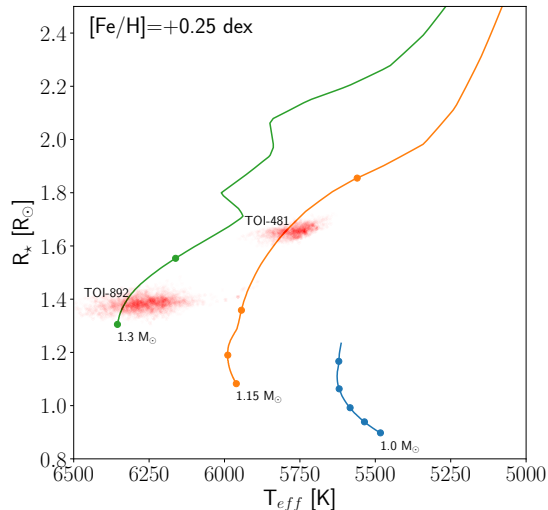


**Figure 6.** Posterior distributions for the effective temperature and stellar radius of TOI-481 and TOI-892 (red clumps). The lines represent PARSEC stellar evolutionary tracks for stellar masses of  $1 M_{\odot}$  (blue),  $1.15 M_{\odot}$  (orange), and  $1.3 M_{\odot}$  (green). A metallicity of  $[\text{Fe}/\text{H}] = +0.25$  is assumed for the three evolutionary tracks, and the circles from bottom to top correspond of the ages of 1, 3, 5, and 7 Gyr.

We analysed the radial velocity time series of both systems to identify variations consistent with the presence of orbiting planets having the periodicity of the transiting candidates. We computed the Generalized Lomb-Scargle periodograms by combining the radial velocities of different instruments for each system. The periodograms are presented in Figure 7 which confirms that both radial velocity sets have significant periodicity at the orbital period of the transiting candidate. The semi-amplitude of these periodic radial velocity variations is consistent with that of giant planets in moderately close-in orbits ( $K \sim 100 \text{ m s}^{-1}$ ).

In order to further confirm that the radial velocity signals are produced by orbiting planets, we analysed the degree of correlation between the radial velocities and line bisector span measurements. We computed the Pearson correlation coefficient with errors through bootstrap finding  $\rho_P = 0.22 \pm 0.19$  and  $\rho_P = -0.19 \pm 0.25$ , for TOI-481 b and TOI-892 b, respectively. Therefore, the absence of significant correlation between radial velocities and line bisector span measurements further supports the hypothesis that the radial velocity variations for both systems are produced by the gravitational pull of transiting giant planets.

### 3.3. Global Modeling

The global modeling of the photometric data and radial velocities for the TOI-481 and TOI-892 systems was performed with the *juliet* package (Espinoza et al.

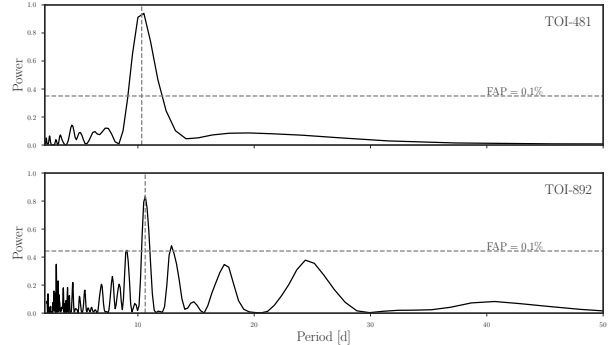


**Figure 7.** Lomb scargle periodograms for the radial velocity time series of TOI-481 (top panel) and TOI-892 (bottom panel). The horizontal dashed line corresponds to the 0.1% false alarm probability. The vertical dashed line corresponds to the period of the transiting candidates.

2018). This package can use either MultiNest (Feroz et al. 2009) through the PyMultiNest package (Buchner et al. 2014) or *dynesty* (Speagle 2020) to perform the posterior sampling via nested sampling algorithms, in order to also compute model comparison through Bayesian model evidences. *juliet* uses *batman* (?) to model the photometric transits, while radial velocities variations are modelled with the *radvel* package (Fulton et al. 2018).

The parameters that were considered for modelling each system are described in the following paragraphs. The photometric and phase folded radial velocity models that were obtained with this process are presented in Figures 3 and 8, respectively, along with the corresponding observations.

#### 3.3.1. Global modelling of the TOI-481 system

For the TOI-481 system, we ran *juliet* fits using *dynesty*, as the number of free parameters (54) needed to account for the global fit is relatively large. In this global fit, we used the Espinoza (2018) parametrization to fit for the planet-to-star radius ratio and the impact parameter. On top of this, we used a prior on the stellar density given by our analysis of the stellar properties in the previous subsection.

For the *TESS* photometry we used a Matérn 3/2 kernel implemented via *celerite* (Foreman-Mackey et al. 2017) to model systematic trends with individual hyperparameters for the amplitude and time-scale of the process for each *TESS* Sector. For the limb-darkening, we assumed a quadratic limb-darkening law parametrized using the non-informative sampling scheme outlined in Kipping (2013). For the short-cadence photometry we assumed unitary dilution factors, as these are already accounted for by the Pre-search Data Conditioning algorithm. For the long-cadence photometry of Sector 3

that was extracted with our own aperture photometry, we considered a dilution factor with a prior between 0.95 and 1. We included photometric jitter terms for each Sector, but the measured jitter was consistent with zero for all but Sector 3. We therefore only fit for photometric jitter in Sector 3 data.

For the CHAT and NGTS photometry, we found no evidence of obvious systematic trends and thus decided to model those datasets as having white-gaussian noise. We used a linear limb-darkening law for both ground-based light curves and we fit for a dilution factor term in the case of the NGTS photometry.

Finally, for the radial velocities we used simple white-gaussian noise models, where each instrument has its own systemic velocity and jitter term. Fits using both eccentric and non-eccentric orbits were performed, with the eccentric model being drastically preferred over the non-eccentric model ( $\ln Z > 5$  in favor of the eccentric model). The final posterior parameters of the global analysis of TOI-481 b are presented in Table 4, along with the prior distributions used for each parameter.

By combining the stellar properties of TOI-481 with the posterior parameters of the adopted `juliet` fit, we find that TOI-481 b has a mass of  $M_P = 1.53^{+0.03}_{-0.03} M_J$ , a radius of  $R_P = 0.99^{+0.01}_{-0.01} R_J$ , a time averaged equilibrium temperature (Méndez & Rivera-Valentín 2017) of  $T_{\text{eq}} = 1370^{+10}_{-10}$  K (partial heat distribution of  $\beta=0.5$  and bond Albedo  $A = 1$ ), and an orbital eccentricity of  $e = 0.153^{+0.006}_{-0.007}$ .

### 3.3.2. Global modelling of the TOI-892 system

For the TOI-892 system we ran two `juliet` fits using `PyMultiNest`, as the number of free parameters (19) is much smaller in this case; one with the eccentricity and argument of the periastron as free parameters, and another one with those values fixed to 0. In both cases for modeling the `tesseract` light curve we adopted the quadratic law for the limb darkening, and a gaussian process with a Matern 3/2 Kernel to model the out of transit variations. For the MEarth and CHAT light curves we adopted a linear limb darkening law. For the radial velocities we considered independent zero points and jitter terms for each spectrograph. We found that the joint modeling with zero eccentricity delivers a higher log evidence than the eccentric version, and we adopted the posterior parameters of that model, which are presented in Table 5 along with the derived planet parameters.

By combining the posterior parameters of the adopted joint fit with the stellar properties of TOI-892 we find that TOI-892 b has a mass of  $M_P = 0.95^{+0.07}_{-0.07} M_J$ , a radius of  $R_P = 1.07^{+0.02}_{-0.02} R_J$ , and an equilibrium tem-

perature of  $T_{\text{eq}} = 1397^{+40}_{-40}$  K. We determine a 98% upper limit for the orbital eccentricity of TOI-892 b of 0.125.

**Table 4.** Prior and posterior parameters of the global analysis of TOI-481 b. For the priors,  $N(\mu, \sigma)$  stands for a normal distribution with mean  $\mu$  and standard deviation  $\sigma$ ,  $U(a, b)$  stands for a uniform distribution between  $a$  and  $b$ , and  $LU(a, b)$  stands for a log-uniform prior defined between  $a$  and  $b$ .

<sup>a</sup> These parameters correspond to the parametrization presented in Espinoza (2018) for sampling physically possible combinations of  $b$  and  $R_P/R_\star$ .

<sup>b</sup> Time-averaged equilibrium temperature computed according to equation 16 of Méndez & Rivera-Valentín (2017).

| Parameter   | Prior                 | Value                              |
|---|-----------------------|------------------------------------|
| P ..... (days)                                      | $N(10.331, 0.1)$      | $10.33111^{+0.00002}_{-0.00002}$   |
| $T_0$ ..... (BJD)                                   | $N(2458511.641, 0.1)$ | $2458511.6418^{+0.0002}_{-0.0002}$ |
| $\rho_\star$ ..... ( $\text{g cm}^{-3}$ )           | $U(0.36, 0.01)$       | $12.52^{+0.03}_{-0.04}$            |
| $r1^a$ .....  | $U(0, 1)$             | $0.32^{+0.04}_{-0.04}$             |
| $r2^a$ .....  | $U(0, 1)$             | $0.1228^{+0.0005}_{-0.0004}$       |
| K ..... ( $\text{m s}^{-1}$ )                       | $U(0, 1000)$          | $130.3^{+1.4}_{-1.4}$              |
| $\sqrt{e} \sin \omega$ .....                        | $U(-1, 1)$            | $0.354^{+0.009}_{-0.010}$          |
| $\sqrt{e} \cos \omega$ .....                        | $U(-1, 1)$            | $0.17^{+0.01}_{-0.01}$             |
| $q_1^{\text{TESS}}$ .....                           | $U(0, 1)$             | $0.64^{+0.06}_{-0.06}$             |
| $q_2^{\text{TESS}}$ .....                           | $U(0, 1)$             | $0.11^{+0.03}_{-0.03}$             |
| $q_1^{\text{CHAT}}$ .....                           | $U(0, 1)$             | $0.55^{+0.08}_{-0.08}$             |
| $q_1^{\text{NGTS}}$ .....                           | $U(0, 1)$             | $0.96^{+0.003}_{-0.04}$            |
| $\sigma_w^{\text{TESS-S3}}$ ..... (ppm)             | $LU(10^{-2}, 10^3)$   | $459^{+8}_{-9}$                    |
| $\sigma_w^{\text{CHAT}}$ ..... (ppm)                | $LU(10^{-2}, 10^4)$   | $2815^{+95}_{-96}$                 |
| $mflux^{\text{TESS-S3}}$ .....                      | $N(0, 0.1)$           | $-0.00001^{+0.00005}_{-0.00005}$   |
| $mflux^{\text{TESS-S6}}$ .....                      | $N(0, 0.1)$           | $-0.0000006^{+0.00005}_{-0.00005}$ |
| $mflux^{\text{TESS-S7}}$ .....                      | $N(0, 0.1)$           | $0.00001^{+0.00004}_{-0.00004}$    |
| $mflux^{\text{TESS-S9}}$ .....                      | $N(0, 0.1)$           | $-0.00004^{+0.00003}_{-0.00002}$   |
| $mflux^{\text{TESS-S10}}$ .....                     | $N(0, 0.1)$           | $-0.00003^{+0.00003}_{-0.00003}$   |
| $mflux^{\text{TESS-S13}}$ .....                     | $N(0, 0.1)$           | $0.001^{+0.004}_{-0.001}$          |
| $mflux^{\text{CHAT}}$ .....                         | $N(0, 0.1)$           | $-0.0019^{+0.0001}_{-0.0002}$      |
| $mflux^{\text{NGTS}}$ .....                         | $N(0, 0.1)$           | $0.00004^{+0.00007}_{-0.00007}$    |
| $dilution^{\text{TESS-S3}}$ ....                    | $U(0.95, 1.0)$        | $0.982^{+0.004}_{-0.005}$          |
| $dilution^{\text{NGTS}}$ .....                      | $U(0.95, 1.0)$        | $0.995^{+0.003}_{-0.003}$          |
| $\gamma^{\text{CHIRON}}$ .... ( $\text{m s}^{-1}$ ) | $N(0, 50)$            | $41.1^{+1.4}_{-1.3}$               |
| $\gamma^{\text{CORALIE}}$ ... ( $\text{m s}^{-1}$ ) | $N(37800, 50)$        | $37808.2^{+2.2}_{-2.2}$            |
| $\gamma^{\text{FEROS}}$ .... ( $\text{m s}^{-1}$ )  | $N(37800, 50)$        | $37797.1^{+1.7}_{-1.6}$            |
| $\gamma^{\text{MINERVA-3}}$ ( $\text{m s}^{-1}$ )   | $N(0, 50)$            | $-54.5^{+3.4}_{-3.1}$              |
| $\gamma^{\text{MINERVA-4}}$ ( $\text{m s}^{-1}$ )   | $N(0, 50)$            | $27.1^{+2.6}_{-2.5}$               |
| $\gamma^{\text{NRES}}$ ..... ( $\text{m s}^{-1}$ )  | $N(0, 50)$            | $-0.7^{+6.7}_{-6.8}$               |
| $\sigma^{\text{CHIRON}}$ .... ( $\text{m s}^{-1}$ ) | $LU(0.01, 50)$        | $0.018^{+0.02}_{-0.006}$           |
| $\sigma^{\text{FEROS}}$ .... ( $\text{m s}^{-1}$ )  | $LU(0.01, 50)$        | $4.1^{+1.7}_{-1.3}$                |
| $\sigma^{\text{MINERVA-3}}$ ( $\text{m s}^{-1}$ )   | $LU(0.01, 50)$        | $14.7^{+3.5}_{-2.5}$               |
| $\sigma^{\text{MINERVA-4}}$ ( $\text{m s}^{-1}$ )   | $LU(0.01, 50)$        | $22.4^{+2.3}_{-1.9}$               |
| $\sigma^{\text{NRES}}$ ..... ( $\text{m s}^{-1}$ )  | $LU(0.01, 50)$        | $33^{+10}_{-10}$                   |
| $\sigma_{\text{TESS-3}}^{\text{GP}}$ .....          | $LU(10^{-5}, 10^2)$   | $0.00031^{+0.00003}_{-0.00003}$    |

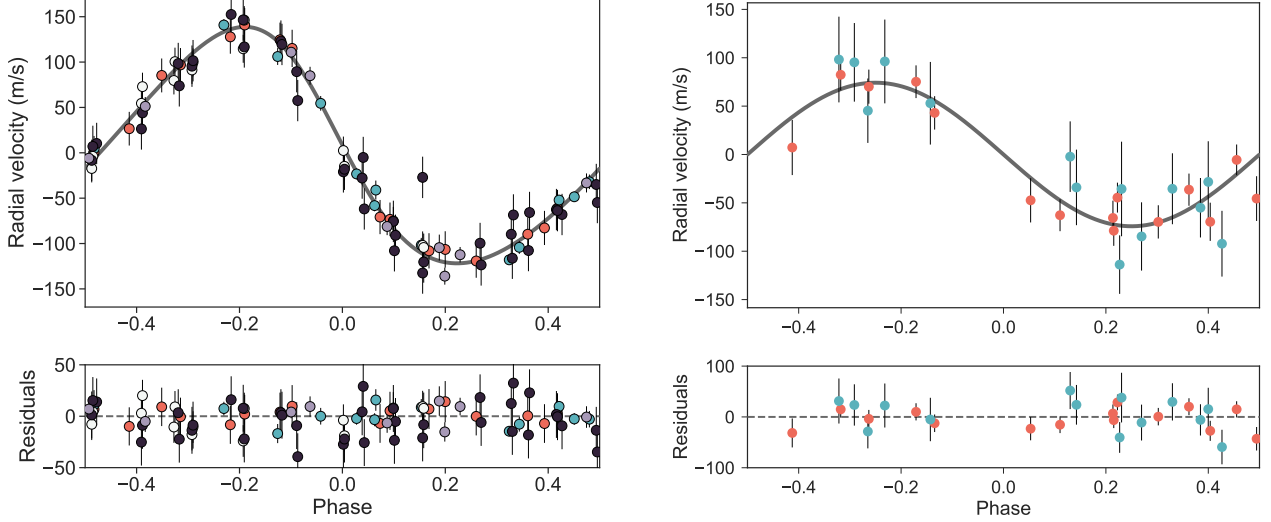


**Figure 8.** The left panel shows the radial velocities of TOI-481 b as a function of the orbital phase. The black line represents the model generated from the posterior distributions obtained in Section 3. The errorbars include the jitter term obtained from the global analysis. The different colors represent the different instruments that were used, namely: FEROS (orange), CHIRON (blue), CORALIE (gray), MINERVA-3 (white), and MINERVA-4 (black). The right panel shows the same but for the FEROS (orange) and TRES (green) velocities of TOI-892 b.

**Table 4.** Continued.

| Parameter                            | Prior               | Value                           |
|--------------------------------------|---------------------|---------------------------------|
| $\sigma_{\text{TESS}-6}^{GP}$ .....  | $LU(10^{-5}, 10^2)$ | $0.00021^{+0.00004}_{-0.00003}$ |
| $\sigma_{\text{TESS}-7}^{GP}$ .....  | $LU(10^{-5}, 10^2)$ | $0.00014^{+0.00003}_{-0.00002}$ |
| $\sigma_{\text{TESS}-9}^{GP}$ .....  | $LU(10^{-5}, 10^2)$ | $0.00018^{+0.00002}_{-0.00002}$ |
| $\sigma_{\text{TESS}-10}^{GP}$ ..... | $LU(10^{-5}, 10^2)$ | $0.00017^{+0.00002}_{-0.00002}$ |
| $\sigma_{\text{TESS}-13}^{GP}$ ..... | $LU(10^{-5}, 10^2)$ | $0.003^{+0.005}_{-0.002}$       |
| $\rho_{\text{TESS}-3}^{GP}$ .....    | $LU(10^{-2}, 10^2)$ | $0.37^{+0.07}_{-0.05}$          |
| $\rho_{\text{TESS}-6}^{GP}$ .....    | $LU(10^{-2}, 10^2)$ | $0.95^{+0.21}_{-0.16}$          |
| $\rho_{\text{TESS}-7}^{GP}$ .....    | $LU(10^{-2}, 10^2)$ | $0.9^{+0.3}_{-0.2}$             |
| $\rho_{\text{TESS}-9}^{GP}$ .....    | $LU(10^{-2}, 10^2)$ | $0.35^{+0.05}_{-0.05}$          |
| $\rho_{\text{TESS}-10}^{GP}$ .....   | $LU(10^{-2}, 10^2)$ | $0.47^{+0.07}_{-0.06}$          |
| $\rho_{\text{TESS}-13}^{GP}$ .....   | $LU(10^{-2}, 10^2)$ | $21^{+23}_{-11}$                |
| b .....                              |                     | $0.15^{+0.05}_{-0.05}$          |
| $R_P/R_*$ .....                      |                     | $0.0614^{+0.0002}_{-0.0002}$    |
| $e$ .....                            |                     | $0.153^{+0.006}_{-0.007}$       |
| $\omega$ (deg) .....                 |                     | $64.8^{+1.8}_{-1.8}$            |
| $i$ (deg) .....                      |                     | $89.2^{+0.3}_{-0.3}$            |
| $M_P$ ( $M_J$ ) .....                |                     | $1.53^{+0.03}_{-0.03}$          |
| $R_P$ ( $R_J$ ) .....                |                     | $0.99^{+0.01}_{-0.01}$          |
| $a$ (AU) .....                       |                     | $0.097^{+0.001}_{-0.001}$       |
| $T_{\text{eq}}(\text{K})^b$ .....    |                     | $1370^{+10}_{-10}$              |

### 3.4. Timing of transits and additional photometric signals

We searched for variations in the time of transits of TOI-481 b and TOI-892 b that could originate from

gravitational interactions with other planets in each system. For this procedure we performed independent *juliet* runs for each one of the transits of the *TESS* and follow-up light curves. We fix most of the parameters to those obtained in the global analysis, but allowed the time of transit and the transit depth to vary. The transit timing variations for TOI-481 b and TOI-892 b are displayed in Figure 9. No significant variations in the timing of transits are identified for both systems.

We also searched for additional transiting candidates in the *TESS* data of both systems by masking out the transits of TOI-481 b and TOI-892 b, and running the box least squares (Kovács et al. 2002) algorithm. No significant signals were identified.

## 4. DISCUSSION

TOI-481 b and TOI-892 b are both compared in Figure 10 with the population of well characterized transiting giant planets ( $M_P > 0.1 M_J$ ) in the planetary radius versus orbital period space. Both planets join the population of moderately long period ( $P > 10$  days) giant planets, which has just recently started to see an increase in the number of detected systems. In terms of physical and orbital properties TOI-481 b is similar to WASP-134 b ( $M_P = 1.41 \pm 0.08 M_J$ ,  $R_P = 0.99 \pm 0.06 R_J$ ,  $P = 10.2$  days, Anderson et al. 2018). On the other hand, TOI-892 b shares similar properties with WASP-185 b (Hellier et al. 2019), that has a mass of  $M_P = 0.98 \pm 0.06 M_J$ , a radius of  $R_P = 1.25 \pm 0.08 R_J$  and an orbital period of  $P = 9.4$  days, but as opposed to

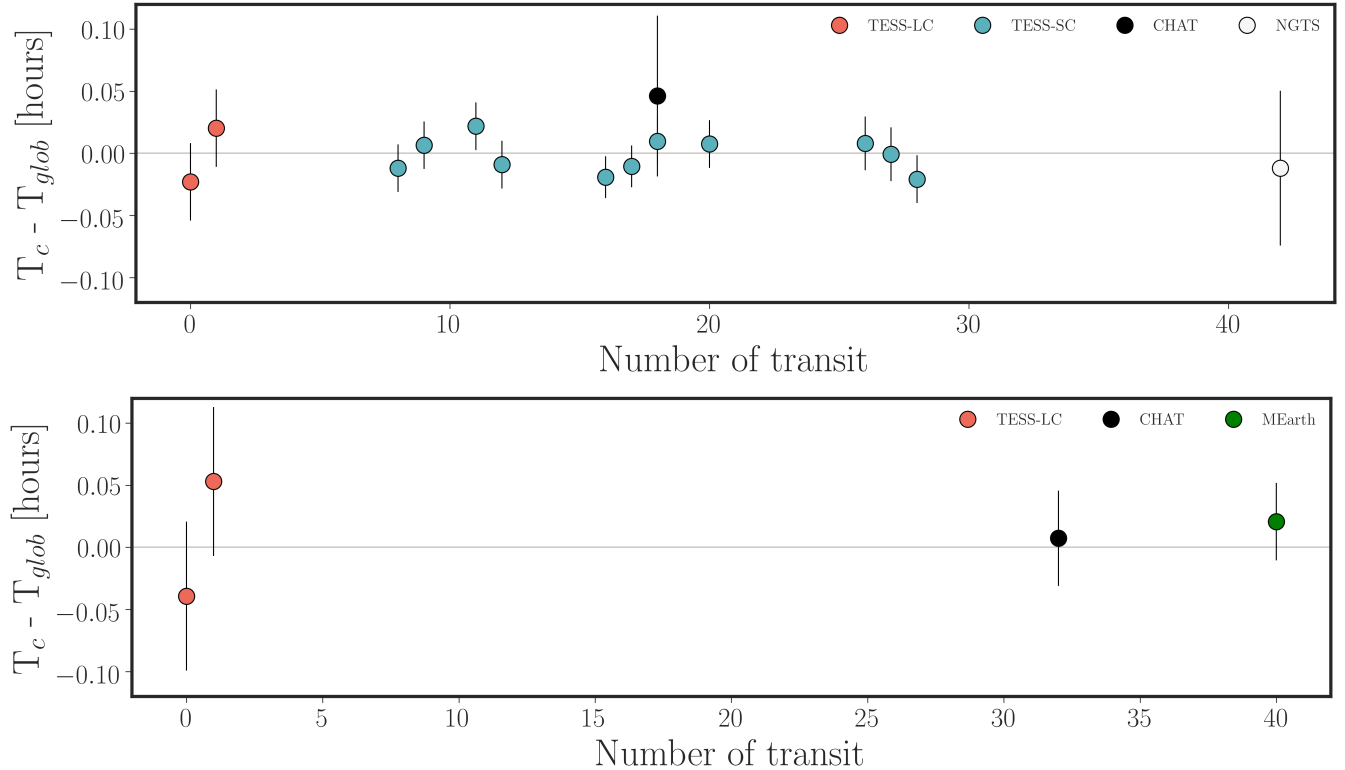


**Figure 9.** Transit timing variations for TOI-481 b (top panel) and TOI-892 b (bottom panel) computed from the *TESS* and ground-based light curves. No significant signal is identified in both cases.

TOI-892 b has a significantly eccentric orbit ( $e=0.23 \pm 0.04$ ).

Despite having periods longer than 10 days, both TOI-481 b and TOI-892 b have moderately high equilibrium temperatures, due to the high luminosity of their host stars. Their equilibrium temperatures are somewhat higher than 1000 K, and therefore these planets are just in the region where the inflation mechanism of hot Jupiters starts to have an impact on the structure of the planet (Demory & Seager 2011; Laughlin et al. 2011). The measured radius for TOI-892 b is in good agreement with the mean radius of other hot Jupiters having similar insolation levels, which is of  $1.1 \pm 0.1 R_J$  for  $1300 < T_{\text{eq}} < 1500$ . The radius of TOI-481 b while still consistent with this distribution, is significantly more compact than that of TOI-892 b. In this context it is important to note that TOI-481 is in the final stages of the main sequence evolution and has started to receive increased levels of irradiation during the last Gyr of evolution. Its non-inflated radius can be linked with a shallow level deposition of the stellar energy into the planet interior during main sequence evolution as argued by Komacek et al. (2020), which is not enough to re-inflate the planet even at temperatures higher than 1000 K. If warm Jupiters are efficiently re-inflated during post-main sequence evolution, as some recent stud-

ies have proposed (Grunblatt et al. 2016; Jones et al. 2018; Grunblatt et al. 2017), then some other mechanism should operate to allow the deposition of energy deeper in the planet interior.

Both systems are well suited objects to perform Rossiter-McLaughlin observations (Rossiter 1924; McLaughlin 1924) for measuring their stellar obliquities (e.g., Triaud et al. 2010). Given the properties of each system, we expect them to have Rossiter-McLaughlin signals with semi-amplitudes of  $15 \text{ m s}^{-1}$  and  $47 \text{ m s}^{-1}$ , for TOI-481 b and TOI-892 b, respectively, for aligned orbits, which can be measured with typical facilities having a stabilized high resolution echelle spectrograph. Spin-orbit angles of giant planets with orbital separations larger than  $\gtrsim 0.1 \text{ AU}$  are expected to be particularly useful for constraining migration scenarios, because at these moderately long orbital distances, tidal interactions are not supposed to be strong enough for realigning the rotation of the outer layers of the star with the orbital plane (Albrecht et al. 2012; Dawson 2014). The low eccentricities of the orbits of TOI-481 b and TOI-892 b and the absence of close planet companions, based on the radial velocity and photometric data, points to interactions with the protoplanetary disc as the most probable migration scenario for these systems (Dong et al. 2014).

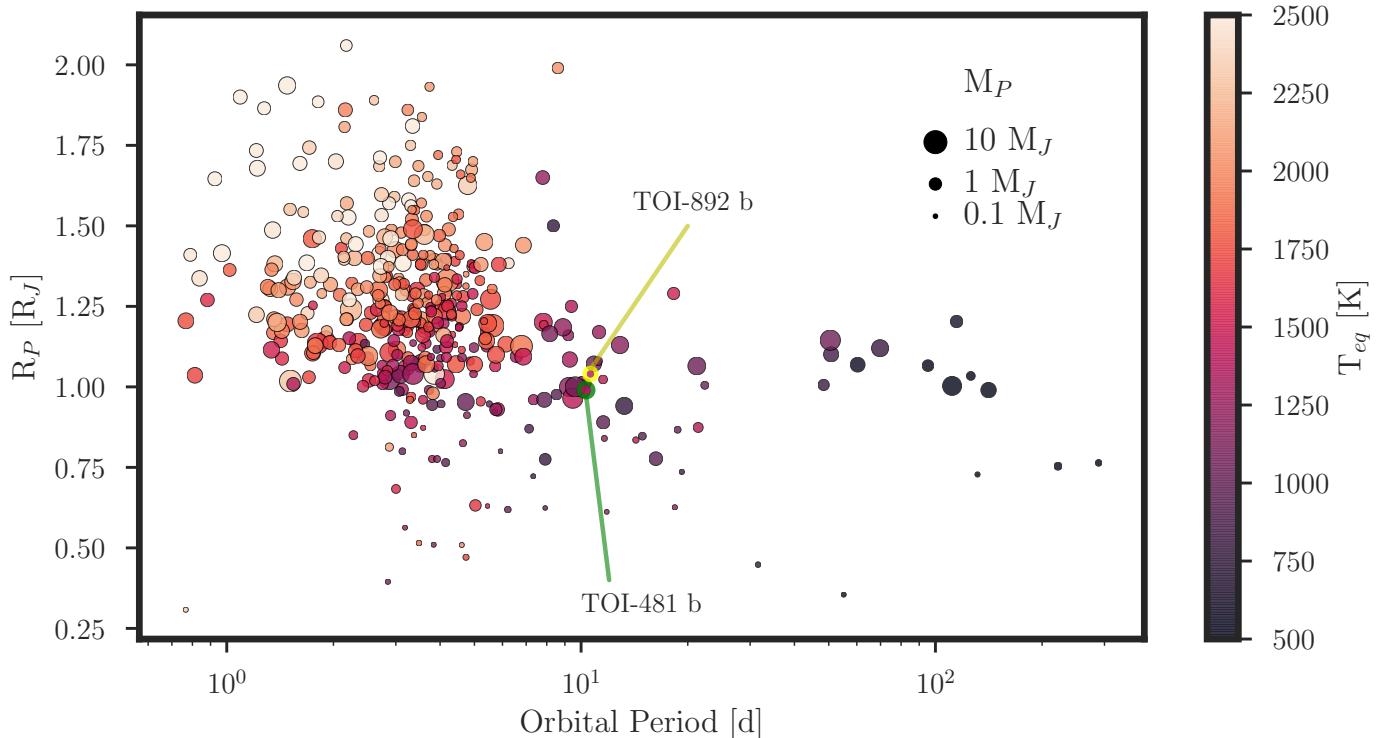


**Figure 10.** Mass–Period diagram for the population of transiting giant planets ( $M_P > 0.1 M_J$ ) having masses and radii measured with a precision of 20% or better. The points are color coded by equilibrium temperature and the pint size scales with the planet mass.

We acknowledge the use of public *TESS* Alert data from pipelines at the *TESS* Science Office and at the *TESS* Science Processing Operations Center. This research has made use of the Exoplanet Follow-up Observation Program website, which is operated by the California Institute of Technology, under contract with the National Aeronautics and Space Administration under the Exoplanet Exploration Program. This paper includes data collected by the *TESS* mission, which are publicly available from the Mikulski Archive for Space Telescopes (MAST). Resources supporting this work were provided by the NASA High-End Computing (HEC) Program through the NASA Advanced Supercomputing (NAS) Division at Ames Research Center for the production of the SPOC data products. R.B. acknowledges support from FONDECYT Post-doctoral Fellowship Project 3180246, and from ANID Millennium Science Initiative ICN12.009. A.J. acknowledges support from FONDECYT project 1171208, and from ANID Millennium Science Initiative ICN12.009.

JIV acknowledges support of CONICYT-PFCHA/Doctorado and Engineering (awarded to D.C.). This material is Nacional-21191829 This work was supported by the DFG Research Unit FOR2544 “Blue Planets around Red Stars”, project no. RE 2694/4-1. We thank Paul Eigenthaler, Angela Hempel, Maren Hempel, Sam Kim

and Régis Lachaume for their technical assistance during the observations at the MPG 2.2 m Telescope. We thank the Swiss National Science Foundation (SNSF) and the Geneva University for their continuous support to our planet search programs. This work has been in particular carried out in the frame of the National Centre for Competence in Research PlanetS supported by the Swiss National Science Foundation (SNSF). MINERVA-Australis is supported by Australian Research Council LIEF Grant LE160100001, Discovery Grant DP180100972, Mount Cuba Astronomical Foundation, and institutional partners University of Southern Queensland, UNSW Sydney, MIT, Nanjing University, George Mason University, University of Louisville, University of California Riverside, University of Florida, and The University of Texas at Austin. This research was supported by Grant No. 2016069 of the United States-Israel Binational Science Foundation (BSF) The MEarth Team gratefully acknowledges funding from the David and Lucile Packard Fellowship for Science and Engineering (awarded to D.C.). This material is based upon work supported by the National Science Foundation under grants AST-0807690, AST-1109468, AST-1004488 (Alan T. Waterman Award), and AST-1616624, and upon work supported by the National

Aeronautics and Space Administration under Grant No. 80NSSC18K0476 issued through the XRP Program. This work is made possible by a grant from the John Templeton Foundation. The opinions expressed in this publication are those of the authors and do not necessarily reflect the views of the John Templeton Foundation. We respectfully acknowledge the traditional custodians of all lands throughout Australia, and recognise their continued cultural and spiritual connection to the land, waterways, cosmos, and community. We pay our deepest respects to all Elders, ancestors and descendants of the Giabal, Jarowair, and Kambuwal nations, upon whose lands the MINERVA-Australis facility at Mt Kent is situated.

*Software:* `juliet` (Espinoza et al. 2018), `CERES` (Brahm et al. 2017a; Jordán et al. 2014), `ZASPE` (Brahm et al. 2017b, 2015), `radvel` (Fulton et al. 2018), `emcee` (Foreman-Mackey

et al. 2013), MultiNest (Feroz et al. 2009), `batman` (?), `SPC` (Buchhave et al. 2012), `SpecMatch` (Yee et al. 2017)

*Facilities:* *Astrometry:* Gaia (Gaia Collaboration et al. 2016, 2018). *Imaging:* SOAR (HRCam; Tokovinin 2018). *Spectroscopy:* CTIO1.5m (CHIRON; Tokovinin et al. 2013), MPG2.2m (FEROS; Kaufer et al. 1999), Euler1.2m (CORALIE; Mayor et al. 2003), Tillinghast1.5m (TRES) (Fűrész 2008), MINERVA-Australis (Addison et al. 2019), NRES (Siverd et al. 2018), *Photometry:* CHAT:0.7m, MEarth-South (Irwin et al. 2015), NGTS (Wheatley et al. 2018), TESS (Ricker et al. 2015).

**Table 5.** Same as Table 5, but for TOI-892 b.  $J(a, b)$  stands for a Jeffrey’s prior defined between  $a$  and  $b$ .

| Parameter                                     | Prior                    | Value                            |
|---|--------------------------|----------------------------------|
| P (days)                                      | $N(10.6, 1.0)$           | $10.62656^{+0.00007}_{-0.00007}$ |
| $T_0$ (BJD)                                   | $N(2458475.7, 1.0)$      | $2458475.689^{+0.002}_{-0.002}$  |
| $a/R_\star$                                   | $U(1, 300)$              | $14.2^{+0.8}_{-0.7}$             |
| $R_P/R_\star$                                 | $U(0.0001, 1)$           | $0.079^{+0.001}_{-0.001}$        |
| b   | $U(0, 1)$                | $0.43^{+0.09}_{-0.13}$           |
| K (km s <sup>-1</sup> )                       | $U(0, 1)$                | $0.074^{+0.005}_{-0.005}$        |
| $q_1^{\text{TESS}}$                           | $U(0, 1)$                | $0.4^{+0.2}_{-0.2}$              |
| $q_2^{\text{TESS}}$                           | $U(0, 1)$                | $0.4^{+0.3}_{-0.3}$              |
| $q_1^{\text{CHAT}}$                           | $U(0, 1)$                | $0.6^{+0.2}_{-0.2}$              |
| $q_1^{\text{MEarth}}$                         | $U(0, 1)$                | $0.90^{+0.08}_{-0.13}$           |
| $\sigma_w^{\text{TESS}}$ (ppm)                | $J(10^0, 10^3)$          | $553^{+20}_{-21}$                |
| $\sigma_w^{\text{CHAT}}$ (ppm)                | $J(10^0, 10^3)$          | $1046^{+69}_{-70}$               |
| $\sigma_w^{\text{MEarth}}$ (ppm)              | $J(10^0, 10^3)$          | $869^{+77}_{-77}$                |
| $\gamma_{\text{FEROS}}$ (km s <sup>-1</sup> ) | $N(42.02, 0.010)$        | $42.033^{+0.005}_{-0.005}$       |
| $\gamma_{\text{TRES}}$ (km s <sup>-1</sup> )  | $N(0.04, 0.010)$         | $0.05^{+0.01}_{-0.01}$           |
| $\sigma_{\text{FEROS}}$ (km s <sup>-1</sup> ) | $N(0.001, 0.1)$          | $0.012^{+0.006}_{-0.006}$        |
| $\sigma_{\text{TRES}}$ (km s <sup>-1</sup> )  | $N(0.001, 0.1)$          | $0.005^{+0.010}_{-0.003}$        |
| $\sigma_{\text{TESS}}^{\text{GP}}$            | $J(10^{-5}, 10^3)$       | $363^{+70}_{-51}$                |
| $\rho_{\text{TESS}}^{\text{GP}}$              | $J(10^{-5}, 10^3)$       | $0.6^{+0.2}_{-0.2}$              |
| $e$   | < 0.125 (98% confidence) |                                  |
| $i$ (deg)                                     |                          | $88.2^{+0.3}_{-0.5}$             |
| $\rho_\star$ (Kg m <sup>-3</sup> )            |                          | $482^{+82}_{-72}$                |
| $M_P$ (M <sub>J</sub> )                       |                          | $0.95^{+0.07}_{-0.07}$           |
| $R_P$ (R <sub>J</sub> )                       |                          | $1.07^{+0.02}_{-0.02}$           |
| $a$ (AU)                                      |                          | $0.092^{+0.005}_{-0.005}$        |
| $T_{\text{eq}}$ (K)                           |                          | $1397^{+40}_{-40}$               |



## REFERENCES

- Addison, B., Wright, D. J., Wittenmyer, R. A., et al. 2019, *PASP*, 131, 115003
- Addison, B. C., Wright, D. J., Nicholson, B. A., et al. 2020, arXiv e-prints, arXiv:2001.07345
- Albrecht, S., Winn, J. N., Johnson, J. A., et al. 2012, *ApJ*, 757, 18
- Almenara, J. M., Díaz, R. F., Hébrard, G., et al. 2018, *A&A*, 615, A90
- Anderson, D. R., Bouchy, F., Brown, D. J. A., et al. 2018, arXiv e-prints, arXiv:1812.09264
- Auvergne, M., Bodin, P., Boisnard, L., et al. 2009, *A&A*, 506, 411
- Bakos, G., Noyes, R. W., Kovács, G., et al. 2004, *PASP*, 116, 266
- Bakos, G. Á., Csubry, Z., Penev, K., et al. 2013, *PASP*, 125, 154
- Barclay, T., Pepper, J., & Quintana, E. V. 2018, *ApJS*, 239, 2
- Barnes, S. I., Gibson, S., Nield, K., & Cochrane, D. 2012, in *Society of Photo-Optical Instrumentation Engineers (SPIE) Conference Series*, Vol. 8446, Proc. SPIE, 844688
- Batygin, K., & Brown, M. E. 2010, *ApJ*, 716, 1323
- Beaugé, C., & Nesvorný, D. 2012, *ApJ*, 751, 119
- Bodenheimer, P., Lin, D. N. C., & Mardling, R. A. 2001, *ApJ*, 548, 466
- Bonomo, A. S., Santerne, A., Alonso, R., et al. 2010, *A&A*, 520, A65
- Borucki, W. J., Koch, D., Basri, G., et al. 2010, *Science*, 327, 977
- Brahm, R., Jordán, A., & Espinoza, N. 2017a, *PASP*, 129, 034002
- Brahm, R., Jordán, A., Hartman, J., & Bakos, G. 2017b, *MNRAS*, 467, 971
- Brahm, R., Jordán, A., Hartman, J. D., et al. 2015, *AJ*, 150, 33
- Brahm, R., Espinoza, N., Jordán, A., et al. 2018, *MNRAS*, 477, 2572
- . 2019, *AJ*, 158, 45
- Bressan, A., Marigo, P., Girardi, L., et al. 2012, *MNRAS*, 427, 127
- Brown, T. M., Baliber, N., Bianco, F. B., et al. 2013, *Publications of the Astronomical Society of the Pacific*, 125, 1031
- Bryant, E. M., Bayliss, D., McCormac, J., et al. 2020, *MNRAS*, 494, 5872
- Buchhave, L. A., Bakos, G. Á., Hartman, J. D., et al. 2010, *ApJ*, 720, 1118
- Buchhave, L. A., Latham, D. W., Johansen, A., et al. 2012, *Nature*, 486, 375
- Buchner, J., Georgakakis, A., Nandra, K., et al. 2014, *A&A*, 564, A125
- Castelli, F., & Kurucz, R. L. 2003, in *IAU Symposium*, Vol. 210, *Modelling of Stellar Atmospheres*, ed. N. Piskunov, W. W. Weiss, & D. F. Gray, A20
- Charbonneau, D., Brown, T. M., Noyes, R. W., & Gilliland, R. L. 2002, *ApJ*, 568, 377
- Cooke, B. F., Pollacco, D., & Bayliss, D. 2019, *A&A*, 631, A83
- Dawson, R. I. 2014, *ApJL*, 790, L31
- Dawson, R. I., & Johnson, J. A. 2018, arXiv e-prints, arXiv:1801.06117
- Deeg, H. J., Moutou, C., Erikson, A., et al. 2010, *Nature*, 464, 384
- Demory, B.-O., & Seager, S. 2011, *ApJS*, 197, 12
- Dong, S., Katz, B., & Socrates, A. 2014, *ApJL*, 781, L5
- Engel, M., Shahaf, S., & Mazeh, T. 2017, *PASP*, 129, 065002
- Espinoza, N. 2018, *Research Notes of the American Astronomical Society*, 2, 209
- Espinoza, N., Kossakowski, D., & Brahm, R. 2018, arXiv e-prints, arXiv:1812.08549
- Espinoza, N., Hartman, J. D., Bakos, G. Á., et al. 2019, *AJ*, 158, 63
- Feroz, F., Hobson, M. P., & Bridges, M. 2009, *MNRAS*, 398, 1601
- Fűrész, G. 2008, PhD thesis, University of Szeged, Hungary
- Foreman-Mackey, D., Agol, E., Ambikasaran, S., & Angus, R. 2017, *AJ*, 154, 220
- Foreman-Mackey, D., Hogg, D. W., Lang, D., & Goodman, J. 2013, *PASP*, 125, 306
- Fulton, B. J., Petigura, E. A., Blunt, S., & Sinukoff, E. 2018, *PASP*, 130, 044504
- Gaia Collaboration, Brown, A. G. A., Vallenari, A., et al. 2018, arXiv e-prints, arXiv:1804.09365
- . 2016, *A&A*, 595, A2
- Gaudi, B. S., Seager, S., & Mallen-Ornelas, G. 2005, *ApJ*, 623, 472
- Gill, S., Wheatley, P. J., Cooke, B. F., et al. 2020, arXiv e-prints, arXiv:2005.00006
- Grunblatt, S. K., Huber, D., Gaidos, E. J., et al. 2016, *AJ*, 152, 185
- Grunblatt, S. K., Huber, D., Gaidos, E., et al. 2017, *AJ*, 154, 254
- Hébrard, G., Ehrenreich, D., Bouchy, F., et al. 2011, *A&A*, 527, L11
- Hellier, C., Anderson, D. R., Barkaoui, K., et al. 2019, *MNRAS*, 490, 1479

- Howell, S. B., Sobek, C., Haas, M., et al. 2014, *Publications of the Astronomical Society of the Pacific*, 126, 398
- Huang, X., Burt, J., Vanderburg, A., et al. 2019, in *American Astronomical Society Meeting Abstracts*, Vol. 233, *American Astronomical Society Meeting Abstracts #233*, 209.08
- Huber, D., Chaplin, W. J., Chontos, A., et al. 2019, *AJ*, 157, 245
- Husser, T. O., Wende-von Berg, S., Dreizler, S., et al. 2013, *A&A*, 553, A6
- Irwin, J. M., Berta-Thompson, Z. K., Charbonneau, D., et al. 2015, in *Cambridge Workshop on Cool Stars, Stellar Systems, and the Sun*, Vol. 18, *18th Cambridge Workshop on Cool Stars, Stellar Systems, and the Sun*, 767–772
- Jenkins, J. M., Twicken, J. D., McCauliff, S., et al. 2016, in *Society of Photo-Optical Instrumentation Engineers (SPIE) Conference Series*, Vol. 9913, *Proc. SPIE*, 99133E
- Jones, M. I., Brahm, R., Espinoza, N., et al. 2018, *A&A*, 613, A76
- . 2019, *A&A*, 625, A16
- Jordán, A., Brahm, R., Espinoza, N., et al. 2020, *AJ*, 159, 145
- Jordán, A., Brahm, R., Bakos, G. Á., et al. 2014, *AJ*, 148, 29
- Jordán, A., Brahm, R., Espinoza, N., et al. 2019, *AJ*, 157, 100
- Kaufer, A., Stahl, O., Tubbesing, S., et al. 1999, *The Messenger*, 95, 8
- Kipping, D. M. 2013, *MNRAS*, 435, 2152
- Komacek, T. D., Thorngren, D. P., Lopez, E. D., & Ginzburg, S. 2020, *ApJ*, 893, 36
- Kovács, G., Zucker, S., & Mazeh, T. 2002, *A&A*, 391, 369
- Kreidberg, L., Line, M. R., Bean, J. L., et al. 2015, *ApJ*, 814, 66
- Kurokawa, H., & Inutsuka, S.-i. 2015, *ApJ*, 815, 78
- Laughlin, G., Crismani, M., & Adams, F. C. 2011, *ApJL*, 729, L7
- Leconte, J., Chabrier, G., Baraffe, I., & Levrard, B. 2010, *A&A*, 516, A64
- Li, J., Tenenbaum, P., Twicken, J. D., et al. 2019, *PASP*, 131, 024506
- Lopez, E. D., & Fortney, J. J. 2016, *ApJ*, 818, 4
- Mayor, M., & Queloz, D. 1995, *Nature*, 378, 355
- Mayor, M., Pepe, F., Queloz, D., et al. 2003, *The Messenger*, 114, 20
- McLaughlin, D. B. 1924, *ApJ*, 60, 22
- Méndez, A., & Rivera-Valentín, E. G. 2017, *ApJL*, 837, L1
- Munari, U., Henden, A., Frigo, A., et al. 2014, *AJ*, 148, 81
- Naoz, S., Farr, W. M., & Rasio, F. A. 2012, *ApJL*, 754, L36
- Nielsen, L. D., Bouchy, F., Turner, O., et al. 2019, *A&A*, 623, A100
- Pepper, J., Pogge, R. W., DePoy, D. L., et al. 2007, *PASP*, 119, 923
- Pollacco, D. L., Skillen, I., Collier Cameron, A., et al. 2006, *PASP*, 118, 1407
- Pont, F., Knutson, H., Gilliland, R. L., Moutou, C., & Charbonneau, D. 2008, *MNRAS*, 385, 109
- Queloz, D., Anderson, D. R., Collier Cameron, A., et al. 2010, *A&A*, 517, L1
- Ricker, G. R., Winn, J. N., Vanderspek, R., et al. 2015, *Journal of Astronomical Telescopes, Instruments, and Systems*, 1, 014003
- Rodriguez, J. E., Quinn, S. N., Huang, C. X., et al. 2019, *AJ*, 157, 191
- Rossiter, R. A. 1924, *ApJ*, 60, 15
- Shporer, A., Zhou, G., Fulton, B. J., et al. 2017, *AJ*, 154, 188
- Siverd, R. J., Brown, T. M., Barnes, S., et al. 2018, in *Society of Photo-Optical Instrumentation Engineers (SPIE) Conference Series*, Vol. 10702, *Proc. SPIE*, 107026C
- Skrutskie, M. F., Cutri, R. M., Stiening, R., et al. 2006, *AJ*, 131, 1163
- Smith, J. C., Stumpe, M. C., Van Cleve, J. E., et al. 2012, *PASP*, 124, 1000
- Southworth, J. 2011, *MNRAS*, 417, 2166
- Speagle, J. S. 2020, *MNRAS*, 493, 3132
- Stassun, K. G., Corsaro, E., Pepper, J. A., & Gaudi, B. S. 2018a, *AJ*, 155, 22
- Stassun, K. G., Oelkers, R. J., Pepper, J., et al. 2018b, *AJ*, 156, 102
- Stumpe, M. C., Smith, J. C., Catanzarite, J. H., et al. 2014, *PASP*, 126, 100
- Stumpe, M. C., Smith, J. C., Van Cleve, J. E., et al. 2012, *PASP*, 124, 985
- Sullivan, P. W., Winn, J. N., Berta-Thompson, Z. K., et al. 2015, *ApJ*, 809, 77
- Thorngren, D. P., Fortney, J. J., Murray-Clay, R. A., & Lopez, E. D. 2016, *ApJ*, 831, 64
- Tokovinin, A. 2018, *PASP*, 130, 035002
- Tokovinin, A., Fischer, D. A., Bonati, M., et al. 2013, *PASP*, 125, 1336
- TriAUD, A. H. M. J., Collier Cameron, A., Queloz, D., et al. 2010, *A&A*, 524, A25
- Twicken, J. D., Catanzarite, J. H., Clarke, B. D., et al. 2018, *PASP*, 130, 064502
- Vidal-Madjar, A., Lecavelier des Etangs, A., Désert, J. M., et al. 2003, *Nature*, 422, 143

- Wang, J., Fischer, D. A., Horch, E. P., & Huang, X. 2015, *ApJ*, 799, 229
- Wang, S., Jones, M., Shporer, A., et al. 2019, *AJ*, 157, 51
- Wheatley, P. J., West, R. G., Goad, M. R., et al. 2018, *MNRAS*, 475, 4476
- Winn, J. N., Johnson, J. A., Howard, A. W., et al. 2010, *ApJL*, 723, L223
- Wu, Y., & Lithwick, Y. 2011, *ApJ*, 735, 109
- Yee, S. W., Petigura, E. A., & von Braun, K. 2017, *ApJ*, 836, 77
- Zhou, G., Huang, C. X., Bakos, G. Á., et al. 2019, *AJ*, 158, 141
- Ziegler, C., Tokovinin, A., Briceño, C., et al. 2020, *AJ*, 159, 19